4 Processes in foaming

> Evolution thus is merely contingent on certain processes articulated by Darwin: variation and selection.
>
> Ernst Mayr, What is Evolution, Science Masters Series/Basic Books, Oct 2001.

4.1 Overview of processes

The evolution of foams occurs through a series of rapid non-equilibrium processes which can be observed by sparging gas through a glass sinter into a column of water. As the air bubbles ascend, their velocities are principally determined by their sizes, the difference in the viscosities of the liquid and gas phases and the properties of the gas/liquid interface. However, as the bubbles grow in size, they may collide and in cases where only weak foaming agents are present in solution, compaction and coalescence can occur. There are several other processes which play an important role in determining the characteristics of the bubbles and the structure of the foam as the bubbles accumulate at the interface. For example, the drainage process or the downward flow of liquid coupled with liquid flow into the Plateau borders can cause thinning of the liquid films. Also, repulsive interactions across the thin film lamellae resulting from strongly adsorbed chemical surfactants can slow down drainage or even prevent bubble coalescence. During the ascent and mixing of bubbles, another important process known as disproportionation occurs. This involves the diffusion of gas from smaller to larger bubbles, and the driving force for this process is the Laplace pressure (the pressure difference between bubbles of different sizes). Although the term "disproportionation" is commonly used by chemists to describe inter-bubble gas diffusion within foams, it is often referred to as Oswald ripening, which was originally used to define the evaporation–condensation mechanism in two-phase separation of binary alloys. The term "coarsening" is often used but coarsening is also frequently considered to be a combination of inter-bubble gas diffusion and coalescence. This confusion in terminology is due to the fact that researchers engaged in foams come from a variety of disciplines, and each has its own terminology. An overview of some of the processes that occur during sparging are outlined in Fig. 4.1.

Molecular processes such as the adsorption and the mobility of chemical surfactant molecules at the air/water interface and also the depletion of surfactant from solution can occur at high gas flow rates can also influence the stability of the bubbles. It is also

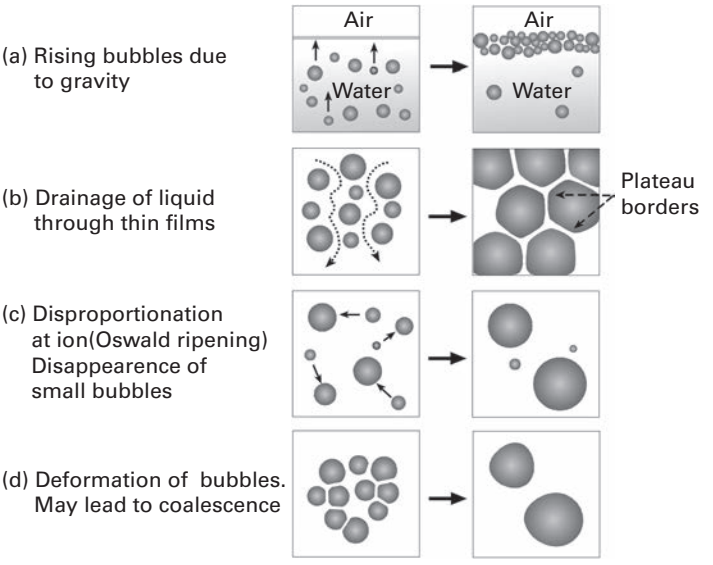

Fig. 4.1 The secondary processes occurring during primary ascent of bubbles to the air/water interface which lead to the formation of a foam.

important to consider the evaporation of liquid from the surface of the foam. Clearly, these processes can occur simultaneously on a similar time scale and are of fundamental importance to the development of the foam structure. However, for simplicity, they will be considered as separate processes in the following sections.

4.2 Ascent of bubbles in liquids

One of the early studies on free rising bubbles in liquids was carried out by Leonardo da Vinci who measured different rates of ascent for bubbles of different sizes. Under the effect of buoyancy, the force (F) which determines the ascent of a free gas bubble in liquid can be expressed by Archimedes law:

$$F = (\pi d^3/6)(\rho_l - \rho_g)g \tag{4.1}$$

where d is the diameter of the bubble, ρ_l is the density of the liquid and ρ_g is the density of the gas. Small bubbles (<0.2 mm diameter) behave similarly to rigid solid spheres in pure water, and according to Stokes law (1880), the terminal velocity (U_{term}) of a rising bubble under a gravitational field is directly proportional to the square of the radius (r) and inversely proportionate to the viscosity of the liquid (η); it can be defined by the equation

$$U_{term} = 2gr^2(\rho_l - \rho_g)/9\eta \tag{4.2}$$

If we assume that the values of the density and the viscosity of the liquid are considerably greater than the gas phase then the bubble ascent velocity can be estimated from

$$U_{\text{term}} = gr^2\rho_l/3\eta \tag{4.3}$$

However, larger bubbles (>0.2 mm) change their shape due to slippage and interfacial mobility. In 1911, Rybczynski (1, 2) modified the Stokes equation and derived theoretical equations for the terminal velocity of flexible bubbles. Following this work, exact analytical solutions to the Stokes equation were published to give more accurate values for the motion of small bubbles (d < 0.01 mm) in pure liquids under creeping flow conditions (with Reynolds number Re <<1) (2). This approach predicts, that due to the fluidity of the bubble, the internal circulation inside the bubble causes the velocity of the bubble to become considerably higher than that predicted by Stokes law for a rigid sphere (with the same diameter and density difference).

Later in 1947, Levich (3) derived a simplified equation for the ascent of a single bubble which is valid for Re < 50 and bubble diameter < 0.5 mm. The Levich equation can be expressed as

$$U_{\text{term}} = gd^2(\rho_l - \rho_g)/36\eta_\ell \tag{4.4}$$

The physico-chemical hydrodynamics of rising bubbles has been well documented in comprehensive reviews by Bikerman (4) and Dukhin and coworkers (5). It is well known that in aqueous solution, containing chemical surfactants or surface active impurities (e.g. in contaminated water) adsorb at the bubble interface as the bubbles ascend, leading to lower mobilities, and theoretical estimates and several explanations have been put forward for this phenomenon. The most important one involves surface tension gradients at the air/solution interface (the Marangoni effect) which occurs as the bubbles rise. This disturbs the equilibrium coverage of the bubbles by chemical surfactant and causes a significant reduction in adsorbed coverage on the upstream part of bubble compared with the lower part. The redistribution of surfactant creates surface tension gradients, and a counter-flow of the interfacial layer from the bottom to the top tends to retard the bubble rise velocity. The situation is illustrated in Fig. 4.2.

Many more advanced theories and models dealing with the effect of adsorbed surfactant layers on the hydrodynamics of bubble motion have been considered, and it is generally accepted that the degree of mobilization depends on the type and amount of adsorbed surfactant. In fact, lack of equilibrium coverage can also cause the surface of the bubble to become unstable and induced surface tension gradient which may cause damping and rapid pulsing of the bubble (shape).

In addition to surface tension gradients, alternative explanations to account for deviation from spherical shape have been discussed by Bikerman (4) – for example, drag forces due to viscous traction and inertia (in the case of larger bubbles) caused by the Laplace pressure. Large bubbles are easily deformed, and the extent of deformation

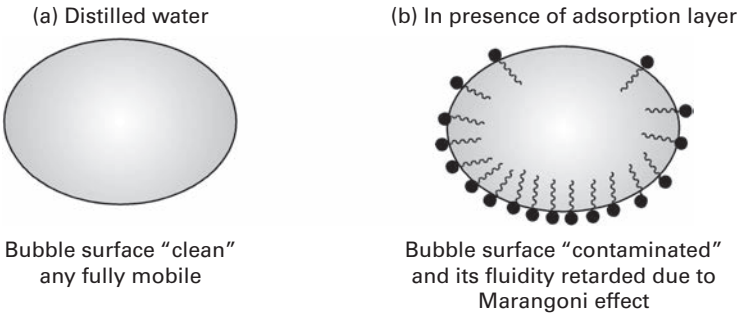

Fig. 4.2 Ascending bubble (a) in water (b) in surfactant solution where the adsorbed surfactant is redistributed along the surface inducing interfacial elasticity.

will depend on the velocity gradient (shear stress). For ascending bubbles in a gravitation field, it is important to take into account the difference in hydrostatic pressure between the top and bottom of the bubble.

4.2.1 Influence of nonionic surfactants

Since 2000, several major achievements have been made in the area of ascending bubbles in aqueous solution, particularly by Malysa and coworkers (6, 7, 8, 9) at the Polish Academy of Science, Cracow. From experimental and theoretical studies, it was possible to determine the influence of different types of chemical surfactants on the bubble ascent velocity, and both the shape (deformation) and the minimum adsorption coverage needed for full immobilization of the bubble interface have been evaluated. It was also shown that the surfactant type and concentration had an important influence on the bubble impact velocity as the bubble reaches the interface as well as on the behavior of the bouncing bubble after the bubble impacted the interface. From the study, it was concluded that the adsorption kinetics had a pronounced influence on the fluidity of the interfacial film. Initially, bubble ascent measurements were made in aqueous solutions of alcohols (pentanol-1, *n*-butanol, *a*-terpineol and *n*-octanoic acid) using a CCD high-speed camera to monitor the shape variation of the bubble (the relationship between the vertical and horizontal diameters) relative to the distance from the capillary. The equipment and method of analysis showing subsequent positions of the bubble are illustrated in Fig. 4.3 and Fig. 4.4.

These experiments revealed that a variation in the shape of the spherical bubble occurred almost immediately after detachment from the capillary, and both the bubble deformation and local bubble velocity were calculated during ascent. Using this procedure, a series of plots of the local velocity of the bubble versus distance from the point of detachment were obtained at a range of alcohol concentrations. A typical set of velocity profiles are shown for *n*-butanol in Fig. 4.5.

These plots clearly show that the concentration of surfactant has a profound effect on the bubble ascent profile. At low and intermediate concentrations, the bubble accelerated

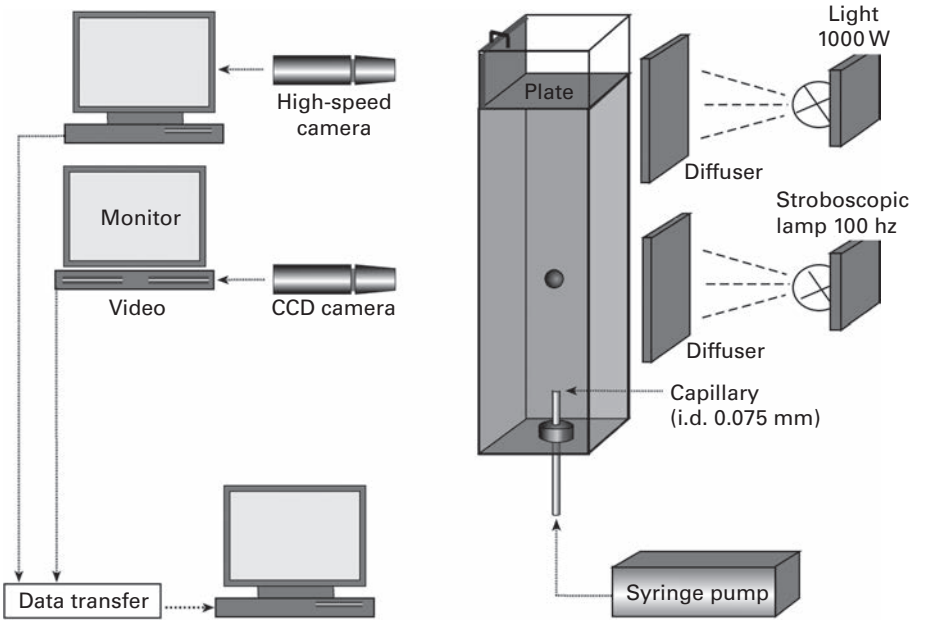

Fig. 4.3 Equipment constructed to record the velocity of rising bubbles. From ref (6).

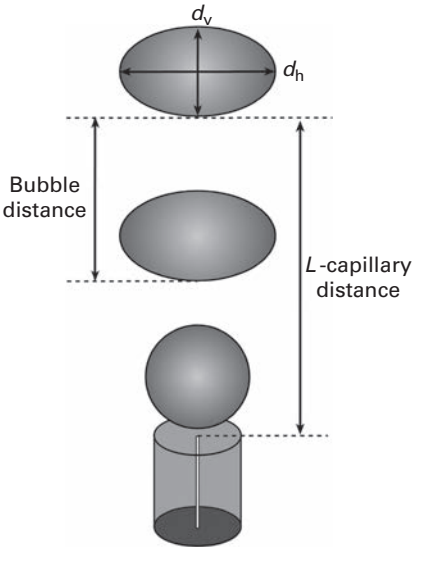

Fig. 4.4 Recorded lengths and distances used to determine the bubble deformation and local velocity. From ref (6).

immediately after detachment, attaining a maximum velocity followed by a monotonic decrease until it reached a constant terminal velocity. Interestingly, at high surfactant concentrations, and also in pure water, no maximum velocity was observed and the bubbles reached their terminal velocity after an initial acceleration step. In order to estimate the amount of surfactant adsorbed on the bubble surface, an elaborate

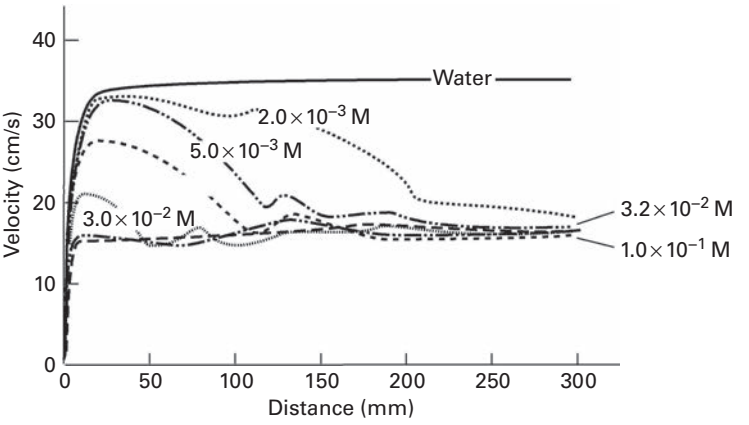

Fig. 4.5 Bubble local velocities as a function of distance from the capillary orifice in *n*-butanol solution at a range of concentrations. From ref (6).

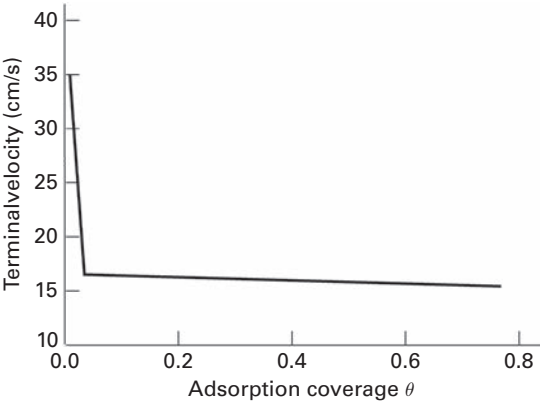

Fig. 4.6 Plots of the dependence of the terminal velocity on adsorption coverage at the surface of the detaching bubble. For n-butanol the data for pentanol-1, *a*-terpineol and *n*-octanoic acid lie on the same two lines. From ref (6).

theoretical model was developed based on a molecular convection/diffusion mechanism and the Frumkin–Hinshelwood adsorption isotherm. This approach enabled plots to be constructed relating the terminal velocity to the adsorption coverage of the bubbles. It was shown that this dependence could be approximated by two lines of very different slopes (as illustrated in Fig. 4.6), and the intersection point of these lines was used to estimate the magnitude of the minimum adsorption coverage needed to immobilize the bubble interface.

From this graph, it can be seen that minimum adsorption coverage has a value of about 0.03 (about 3% of the total adsorption coverage), and in addition, the critical concentration of surfactant could be estimated which corresponded to this minimum coverage. At this point, it could be presumed that sufficient surfactant was adsorbed to produce a coating which immobilized the bubble interface.

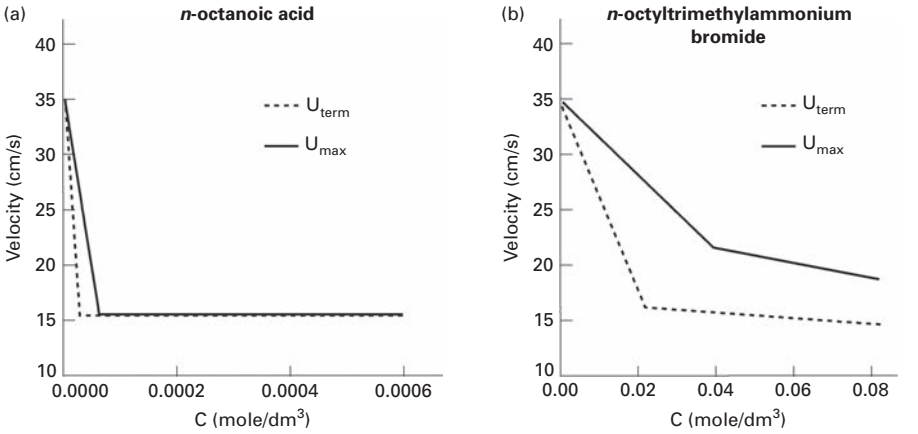

Fig. 4.7 Dependence of the bubble terminal and maximum velocity on concentration (a) *n*-octanoic acid and (b) *n*-octyltrimethylammonium bromide. From ref (7).

4.2.2 Influence of ionic surfactant

Krzan and coworkers (7) extended these studies by investigating the influence of ionic surfactants on the terminal (U_{term}) and maximum (U_{max}) velocities of the bubbles. Experiments, similar to those reported for the alcohols, were carried out using ionic surfactants with different polar groups but identical hydrocarbon chain lengths (C_8). These included *n*-octanoic acid, *n*-octyltrimethylammonium bromide, *n*-octyl dimethylphosphine oxide, *n*-octyl-*β*-D-glucopyranoside. This approach enabled values of U_{term} and U_{max} to be determined as a function of concentration of the ionic surfactants. Comparison plots of the terminal and maximum velocities for an anionic surfactant *n*-octanoic acid and a cationic *n*-octyltrimethylammonium bromide are shown in Fig. 4.7.

It can be seen that in the low-concentration ranges, the initial values of both the terminal velocity and the maximum velocity of the polar surfactants decreased rapidly with concentration; however, further increases in concentration had a less pronounced effect on these values. This is more effective for the more strongly polar cationic surfactants such as the *n*-octyltrimethylammonium bromide (Fig. 4.7b). Although U_{term} reaches U_{max} for the *n*-octanoic acid in the low concentration range, higher amounts were needed to reach this value in the case for *n*-octyltrimethylammonium bromide. However, it was not possible to suggest a complete explanation for this behavior studies suggested that impurities played a role.

From the data, it was found possible to calculate the rising bubble shape deformation (χ which is defined as the ratio of its horizontal and its vertical diameters d_h/d_v as indicated in Fig. 4.4) and the value of the equivalent diameter d_{eq} as expressed by $d_{eq} = (d_v d_h^2)^{1/3}$, where d_v and d_h are the vertical and the horizontal diameters, respectively. The results (Fig. 4.8) relate both the degree of deformation and the equivalent diameter of the bubble to the concentration of the surfactants.

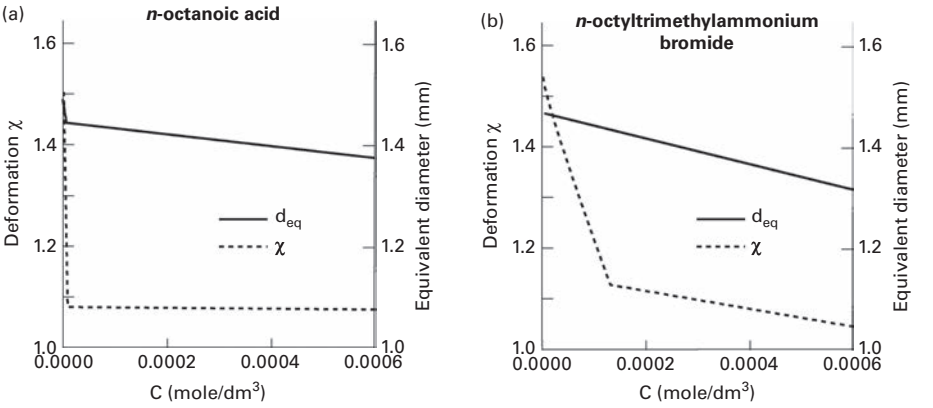

Fig. 4.8 Variations of the equivalent diameter and degree of bubble shape deformation with concentration of (a) *n*-octanoic acid and (b) *n*-octyltrimethylammonium bromide. From ref (7).

In all cases, these results showed that the bubble equivalent diameter diminished almost linearly with concentration; however, this concentration effect had a much more pronounced influence on the shape deformation. Clear differences were seen between the strong and weak polar surfactants, and it was noted that the bubble in distilled water was oblate spheroidal with a horizontal diameter 50% greater than the vertical diameter ($\chi = 1.5$). A profound deformation also occurred at low surfactant concentrations with shape deformation decreasing rapidly at very low ionic concentration values for the *n*-octanoic acid; but with the *n*-octyltrimethylammonium bromide, deformations occurred at higher concentrations. It was suggested that in the case of *n*-octyltrimethyl ammonium bromide in the low concentration range, rapid adsorption/desorption prevented the establishment of a steady-state distribution of the surfactant across the interface of the rising bubble. This prevented the build-up of a surface tension gradient.

4.2.3 Bubbles bouncing from the interface

Experiments carried out in pure water and in aqueous surfactant solutions revealed that when the bubbles reached the air/water interface, they did not burst immediately but remained on the surface and formed a dome (8,9). It was observed that bubbles were rebounding from the interface and pulsating rapidly (the rate of the horizontal/vertical diameters changed rapidly at frequencies greater than 1000 Hz). During successive collisions with the bulk interface, both the velocity of the bouncing bubble and the amplitude of diameter variations were found to decrease (dampened). The final stages of the process resulted in either the formation of a stable film or the rupture of the bubble, and the bubble lifetime was found to vary from a few seconds to tens of minutes. The fact that this behavior occurred both in surfactant solution and in clean water was completely unexpected. In clean water, rapid coalescence was anticipated. The image analysis of the bouncing process is shown in Fig. 4.9.

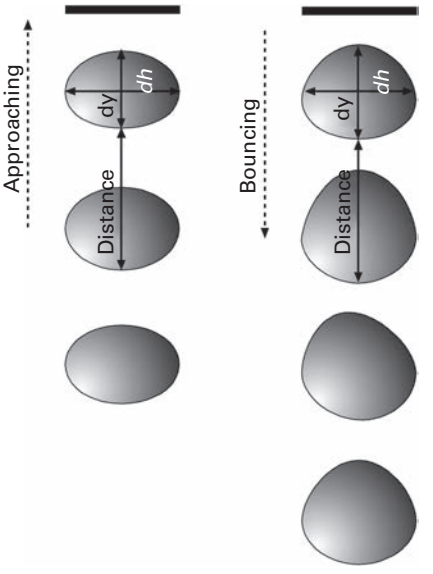

Fig. 4.9 Method of image analysis applied to determine the local velocity of the bubble colliding with the liquid/gas and liquid/solid interfaces. From ref (9).

Film rupture is well known to occur when the water layer above the top pole of the bubble reaches a critical thickness which was dependent on the type and concentration of surfactant. It was proposed that the forces that cause the damping of bubbles and the shape pulsations were caused by the surface tension gradients induced by the bubble motion, which cause flow in the opposite direction to the liquid flow, and these act to prevent the uniform adsorption of surfactant over the deformed interface. In addition, they cause the outward flow of surfactant molecules, and the interfacial elasticity counteracts this outflow and retards the film thinning process. The proposed mechanism is shown in Fig. 4.10.

4.2.4 Influence of impact velocity at the interface

In order to investigate the kinetics of the oscillating and rupture process in more detail, Zawala and Malysa (9) carried out a further series of basic experiments designed so that the bubbles approach the surface at a constant velocity. This was achieved by adjusting the bubble size and the distance between the bubble release point and the interface. In this experiment, both the kinetics of the bouncing and the coalescence processes were recorded. In Fig. 4.11, a typical plot of the kinetics of the bouncing process for the velocity variations of two different sizes bubbles (R_b = 0.5 and 0.74 mm) is shown. The negative velocity values indicate bubble rebound (moved backward in comparison to the approaches to the interface), and t = 0 indicates the occurrence of the first collision; the negative time values indicate the bubble approach stage. Rupture times were found to vary from a few milliseconds to about 120 ms.

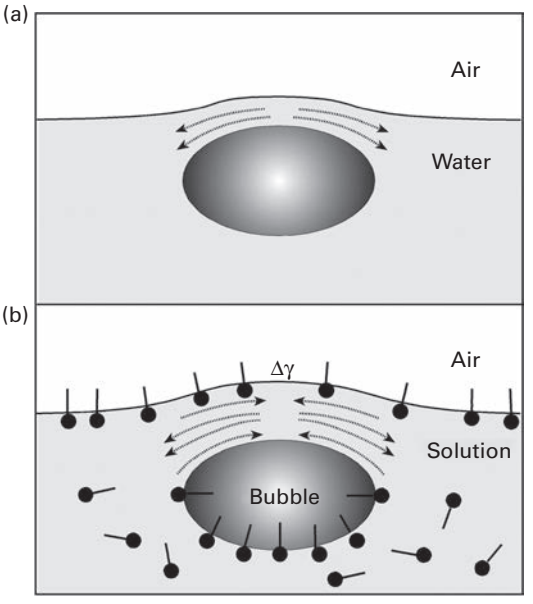

Fig. 4.10 Schematic illustration of the surface tension gradient action during film thinning. From ref (9).

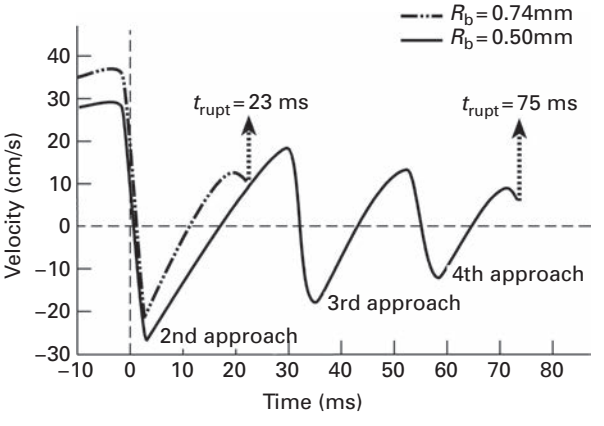

Fig. 4.11 Velocity variations of the bubble of radius R_b = 0.50 and 0.74 mm during bouncing from the water interface. From ref (9).

As anticipated, higher impact velocities caused larger bubble deformation, resulting in an increase in the radius of the liquid film. It was proposed that the bouncing behavior was explained by the fact that there was insufficient time (due to slow drainage) to reach a critical rupture thickness. The number of bounces from the interface increased with impact velocity, and higher impact velocities caused the prolongation of the coalescence time.

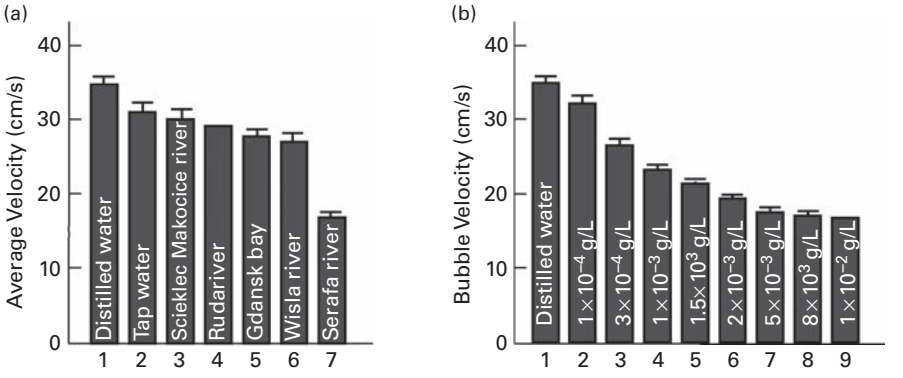

Fig. 4.12 The ascent velocity of bubbles in (a) five environmental water samples collected from Poland and the Baltic Sea and (b) water samples showing the effect of increasing concentrations of surface active impurities. From ref (10).

4.2.5 The detection of surface-active contaminants in water

Finally, Kawala and coworkers (10) utilized the bubble ascent technique as a simple and inexpensive means of detecting surface active organic contaminants in water. A long glass tube was used with a capillary in the base. The ascent velocity of the bubble was measured over a distance of 140 cm in samples of contaminated water and the mean value was determined. From these studies, it was reported that the bubble velocity could be reduced by over 50% due to surface active contaminants, and detergents (dishwashing liquids and washing powder) could be measured. Reference detergents were used for calibration purposes and gave an indication of the levels of contamination. Figure 4.12 shows the application of such a bubble rise technique by comparing five polluted samples with distilled water and tap water (Fig. 4.12a) and the effect of increasing the concentration of surface active pollutant in water (Fig. 4.12b)

4.3 Drainage of foams

Drainage rates give an indication of how long a liquid needs to flow through the channels (PBs) and nodes (intersections of four channels) between bubbles of the foam while experiencing a resistance due to viscous friction from the walls. The main driving forces for foam drainage are gravity and capillary pressure. The drainage can be described as a complex hydrodynamic process governed by laminar flow which acts directly on the film and indirectly through capillary suction, causing the Plateau borders (PBs) to swell. However, these forces are opposed by the surface tension gradient along the air/water interface (the Gibbs–Marangoni effect) and viscous damping. The resulting steady-state flow is obtained by balancing these effects. The simplified situation within a thin film segment with adsorbed surfactant is shown in Fig. 4.13.

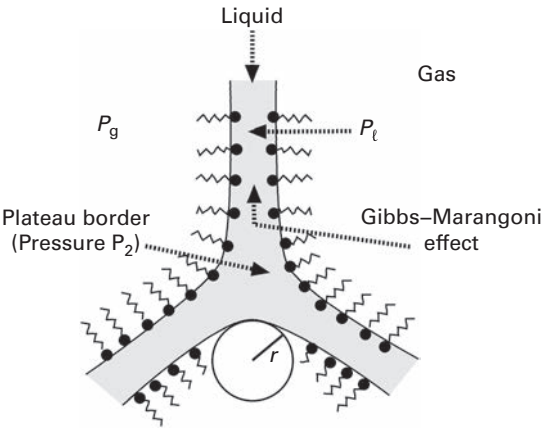

Fig. 4.13 Drainage through a Plateau border. Gravity and capillary forces (causing thinning) are the driving forces, with the Gibbs–Marangoni effect acting as a restoring force by reducing the thinning of the films.

The resulting steady-state flow can be resolved by balancing these effects, and most attempts to analyze this problem have led only to the development of a series of semi-empirical equations, rather than a single equation to describe the entire system. The early background to the derivation of some such drainage equations, and details of the models used, are described by Bikermann (4) and Weaire and Hutzler (11). However, only a few of the early equations have a firm theoretical foundation and, in many cases, it is not clear why the experimental drainage behavior of one foam system agrees with a particular equation compared to another. More recent drainage experiments show that foam drainage depends on many different parameters such as gas type, liquid viscosity, surfactant type, bubble size, liquid fraction, bulk rheology, foam height, foam film type and interfacial properties. In addition, under practical conditions, disproportionation, coalescence and structural rearrangements may occur within the fluid framework and complicate the drainage.

Generally, during the foam drainage process, it is the size and inclination of the PB which influences the bubble shape. Many early researchers modelled systems that assume the foams to have a pentagonal dodecahedral structure while other models have been developed assuming specific shapes for the PB (circular or triangular). Although the PBs have a specific size, a continuum approach is often taken in the modeling, and checks are commonly made to determine the consistency of a model with experimental data. Many of the early models were based on the pioneering work of Leonard and Lemlich (12) in 1965, in which an equation was derived to describe the average linear (Poiseuille-type) flow in a gravitation field across a PB with an immobile (rigid) interface. However, the assumption of non-slip boundary conditions at the walls of each of the PBs is dubious and can only be justified by the presence of high interfacial viscosities resulting from certain types of surfactant systems such as proteins. It is also assumed that the foam has a polyhedral structure, and following this approach,

a standard theory was developed that averaged all possible orientations of the PBs in the foam from which the drainage velocity (V_d) was expressed as

$$V_d = (0.16{R_{pb}}^2/150\eta_\ell)\ (\rho_\ell g) \tag{4.5}$$

where R_{pb} is the PB curvature radius, η_ℓ is the dynamic viscosity and ρ_ℓ is the liquid density. In this regime, the flow is channel-dominated (11, 13, 14). However, in the limiting case of a very mobile surface, dissipation in the modes becomes predominant, and a node-dominated drainage regime predominates. In this case, the drainage velocity can be expressed as

$$V_d = \ (K_n^0\ \rho_\ell g/\eta_\ell)\ ({L_{pb}}^2 {\Phi_l}^{1/2}) \tag{4.6}$$

where K_n^0 is the dimensionless permeability, L_{pb} is the PB length and Φ_l is the liquid volume fraction. Specialized experimental techniques, such as the foam pressure drop technique, have been developed to identify channel- and node-dominated drainage regimes and also the influence of the collapse of the inner foam in the column on drainage (15).

4.3.1 Forced, free and pulsed drainage

In order to characterize the transport of liquid through the foam and relate theoretical models to experimental data, several different types of experiments (forced, free and pulsed drainage) have been used to give different types of drainage profiles, but each relates the volume fraction of the liquid in the foam to the height (distance). Data are frequently recorded after precisely defined time intervals, and typical profiles obtained from these three types of experiments are discussed by Koehler and coworkers (13); an overview is presented schematically in Fig. 4.14. The different stages of such processes are discussed in some detail in the following three sections.

4.3.1.1 Forced drainage

This is a relatively simple, and useful, technique in which a constant controlled amount of solution is continuously introduced (at a constant flow rate) at the top of an initially drained (dry) foam. The drainage profile is characterized by the formation of a well-defined front (a travelling wave) which moves downward at a constant speed, shown in Fig. 4.14(a), where the measured volume fraction profiles correspond to five successive times. In forced drainage, the distinct front does not change in shape with time and moves down with constant velocity, forming solitary a wave. Forced drainage experiments are usually easier to interpret. The downward velocity (constant) of the boundary between dry and wet foams (V_{FD}) can be related to the flow rate (Q) by

$$V_{FD} = BQ^a \tag{4.7}$$

In cases where bubble channel surfaces are rigid, Poiseuille flow occurs through the PBs, which corresponds to $a = ½$, which leads to

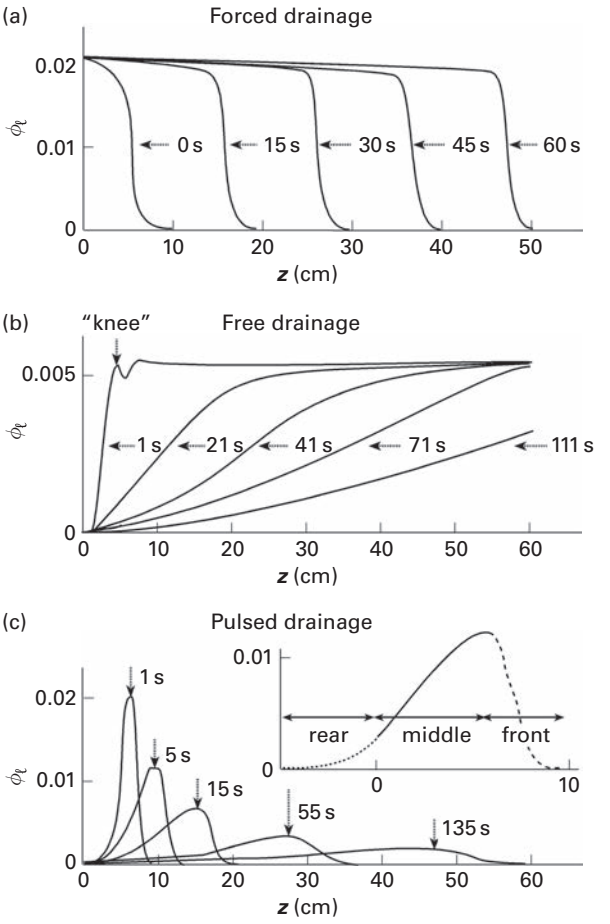

Fig. 4.14 Profiles showing the dynamic of three foam drainage experiments. Liquid volume fraction versus height. The +z-axis is pointing in the direction of gravity (a) forced drainage, (b) free drainage, and (c) pulsed drainage. Each profile is labeled by the time in seconds when it was taken. Horizontal arrows in (a) and (b) show the location of the half-maximum of the profile. The vertical arrow in (b) shows the location of the knee of the pulse at $t = 1$ s. In (c) the arrows show the location of the pulse maximum for five successive profiles. All profiles were averaged over about 1 cm, and for pulsed drainage at longer times over several cm. The inset of (c) shows the three regions of a pulse here for $t = 5$ s. (i) The rear (just above the injection point, (ii) the middle region extending from the injection point to the pulse maximum (solid line) and (iii) the front which is in the region below the pulse max (dashed and dotted line). From ref (13).

$$B = [B_1(\rho_\ell L_{\mathrm{pb}}{}^3/\eta_\ell A_\mathrm{s})]^{1/2} \tag{4.8}$$

where A_s is their sectional area, B_1 is a constant and L_{PB} depends on the bubble size and on the liquid volume fraction.

Experimental studies over the past decades have clearly shown that drainage rates and the associated drainage regime (node or channel) that are governed by the interfacial properties during forced drainage transitions between the two regimes

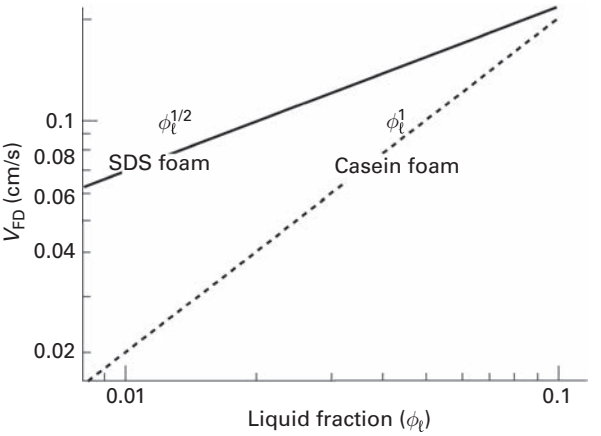

Fig. 4.15 Typical force drainage curves (velocity V_{FD} versus liquid fraction ϕ_ℓ) for foams made from SDS and a casein solution. The bubble size and bulk viscosity are constant and only the interfacial properties differ. From ref (18).

have been well characterized. Durant and coworkers (16) carried out experiments with different surfactants and reported a power law relationship between drainage rates and flow which varied according to the type of surfactant. The results were explained by the transition between node dominated and Plateau border dominated viscous dissipation.

Saint-Jalmes and coworkers (14), in order to carry out forced drainage experiments, used a mixed surfactant system (sodium dodecyl sulfate (SDS)/dodecanol) with different molecular ratios. For small levels of dodecanol, the bubble surface was considered to be mobile, and plug-like flow was detected; but at higher ratios of dodecanol the surface becomes rigid and Poiseuille-like flow was reported. For most protein foams, Poiseuille-like flow predominates. Different drainage regimes were also reported for proteins and sodium lauryl sulfate (17, 18). Protein molecules usually produce interfaces with a high interfacial elasticity and viscosity causing slower drainage compared to low molecular weight surfactants such as SDS. A typical set of data is shown in Fig. 4.15 where the graph relates the liquid velocity to the liquid fraction for milk protein (casein) and SDS foams. Both foam systems were adjusted so that the bubble size and bulk viscosity were constant.

Saint-Jalmes (17) found that for the SDS foam, V_{FD} is proportional to $(\phi_\ell)^{1/2}$ which is consistent with a node-dominated regime where, under steady-state conditions, the drainage can be expressed as

$$V_{FD} = \frac{K_c \rho_\ell g L_{pb}^2}{\eta_\ell} \phi^{1/2} \tag{4.9}$$

For the protein foam, V_{FD} is proportionate ϕ_ℓ and this is consistent with the channel-dominated regime assuming a steady-state liquid fraction and no capillary effects. Under these conditions, the drainage velocity can be expressed as

$$V_{\mathrm{FD}} = \frac{K_{\mathrm{c}} \rho_{\ell} g L_{\mathrm{pb}}^2}{\eta_{\ell}} \phi \tag{4.10}$$

where K_{c} is a dimensionless number describing the PB permeability, L_{pb} is the PB length, ρ_{ℓ} is the solution density and η_{ℓ} is the fluid viscosity.

4.3.1.2 Free drainage

In this case, the foam is generated in a column and, at some interval of time, the bubbling stopped. At this stage, it is assumed that the initial liquid content in the foam is high and uniformly distributed, and it is important that this initial state of the foam is reproducible for direct comparison of modes at time $t = 0$. At this point, the foaming solution is then added to the foam which freely drains through the bubbles. The process is complex and frequent long drainage times are required. It is assumed that the foam remains uniform with a constant liquid fraction all along its height and, as the liquid fraction increases, a knee is formed and the dry foam front can lead to the formation of two overlapping regions in the foam body. The rear and knee regions are shown in Fig. 4.14(b). In the rear region, the liquid volume fraction increases from the top toward the bottom until it reaches a constant value ϕ_{min} in the knee region. The knee moves downward with a constant velocity that is greater than the rear velocity, which causes the rear region to grow with time. This results in a less sharp liquid fraction vertical profile compared to forced drainage, and the front broadens rapidly when it reaches the bottom of the container. It is therefore difficult to measure a precise drainage velocity. However, differences similar to that of forced drainage can be detected between regimes of fluid and rigid interfaces

4.3.1.3 Pulsed drainage

This is a modification of the forced drainage situation; however, a short pulse of the foaming surfactant solution is periodically added onto the top of the foam, as opposed to a constant flow of solution, and this spreads out as it moves down the column. Pulse drainage plots in Fig. 4.14(c) show the evolution of a finite amount of liquid in an otherwise dry foam. As the liquid passes through the foam, the drainage wave profile consists of three regions which are (a) the drained region below the travelling wave wet wave, (b) the transition region in the vicinity of the front of the wet wave and (c) the main body region.

4.3.2 Influence on interfacial properties

Considerable progress has been made during the past two decades in both experimental and theoretical drainage studies, particularly with respect to the influence of the interfacial properties resulting from chemical surfactants and this has led to an improved understanding of foam drainage. In 2008, Kruglyakov and coworkers (19) reviewed several drainage models, both standard and extended, and highlighted the influence of the physico-chemical properties on the gas/liquid interface. Standard drainage theory

has been considerably improved by including the influence of surface viscosity, the surface diffusion and surface tension. And it has also been confirmed that the foam structure plays a critical role in drainage. Experimental results illustrate that variations in physical parameters can cause transitions between node- and channel-dominated regimes. Although a considerable amount of experimental data has been accumulated on foam drainage with various surfactants, it has proved difficult to establish a uniform theory to describe the complete process. However, the results to date have confirmed that changes in surface rheological properties induced by different surfactant type play a key role in foam drainage.

4.3.3 Experimental approaches

In addition to the physico-chemical properties as determined by the surfactant, the height and shape of the foam container, the initial vertical liquid distribution within the foam structure and the number of bubbles at each height have an important influence on drainage. Therefore, the experimental conditions need to be precisely defined. As the liquid drains through the foam structure, the decrease in liquid volume fraction and the increase in the capillary pressure define the bubble size at the various heights of column. The drainage time of the liquid in the foam (t_{dr}) and the velocity of drainage V_d (= $1/t_{dr}$) are variables and depend on a range of parameters. Physicists frequently study the redistribution of liquid in the PBs and nodes during drainage, and several different experimental techniques have been reported which enable the drainage rate to be determined. These include NMR, ESR and chemical dye techniques. Koehler and coworkers (13) carried out detailed drainage experiments using a foam prepared with a gas with a low diffusion coefficient (C_2F_6) and monodispersed bubbles to avoid disproportionation and used a good foaming surfactant to ensure a highly stabilized foam system. Fluorescence dye was used in the experiments to determine the spatial and temporal variations of the liquid volume fraction in aqueous foams. From the data, a generalized drainage model was developed that took account of viscous dissipation in both channels and nodes of the liquid network. By using this model, good agreement was obtained with the experimental results obtained for all three types of drainage.

4.3.4 Influence of foam film type

Early fundamental experiments in the 1960s with single isolated thin films were carried out by the Bulgarian Research group (20), who indicated that different types of foam films (CTF, CBF or NBF) exhibited different drainage rates. Later, follow-up studies around 1995, with an experimental cell constructed by Khristov and Exerowa (21), enabled more precise hydrodynamic investigations to be carried out on foam systems constructed from CTF, CBFs and NBFs. A schematic diagram of the equipment is shown in Fig. 4.16.

The measuring cell was fitted with a porous plate base and the foam is generated to a pre-set level. Initially, a stopcock connected to vacuum enabled the pressure

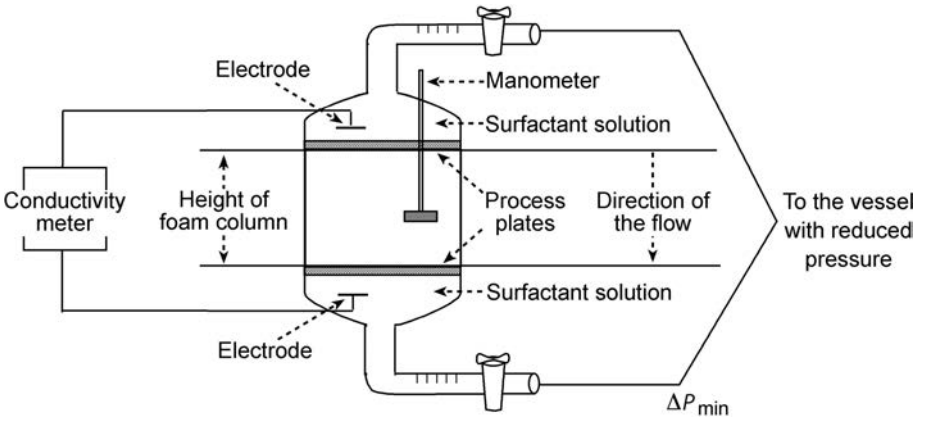

Fig. 4.16 Schematic diagram of the apparatus used in the study of the process of foam drainage with different types of thin films. From ref (21).

above the foam to be reduced while two different types of electrodes – horizontal and vertical – were constructed within the cell. For each series of experiments, the drainage rate was regulated by controlling the pressure difference ΔP. During the drainage process, the rate was monitored by electroconductivity, and the liquid content of the foam (W_l) was calculated by substituting the values of the electroconductivity of the foam K_f in the standard foam conductivity equation:

$$W_l(\text{vol}\%) = B_3(K_f K_s) \times 100 \tag{4.11}$$

where K_s is the specific conductivity of the bulk solution and B_3 is a proportionality coefficient accounting for the distribution of the liquid between the PBs and the foam films, which is dependent on the foam structure.

Foams usually drain slowly under gravity, but using the porous plate apparatus the drainage rates can be accelerated by applying an increased and regulated pressure to the foam liquid phase. In addition, coalescence and drainage can be studied independently. Experiments were reported for solutions of SDS with the addition of different concentrations of sodium chloride (C_{el}) to regulate the ionic strength. This enabled different types of foam film systems to be evaluation, and the critical electrolyte concentration that corresponded to the CBF/NBF transition could be determined. A typical set of drainage curves is shown in Fig. 4.17 for three different types of foams with different thin films. The log W/t curves present the rate of foam drainage for the three types of films. The differences in drainage rates in these systems are evident. The slowest rate of drainage is observed in foams with CTF while foams with NBF and CBF it increases considerably and the highest rate with CBF until an equilibrium state is reached. The values of W at which a plateau begins are also different for the three curves, and the plateau occurs when the capillary pressure and applied pressure become equal by establishing a hydrostatic equilibrium.

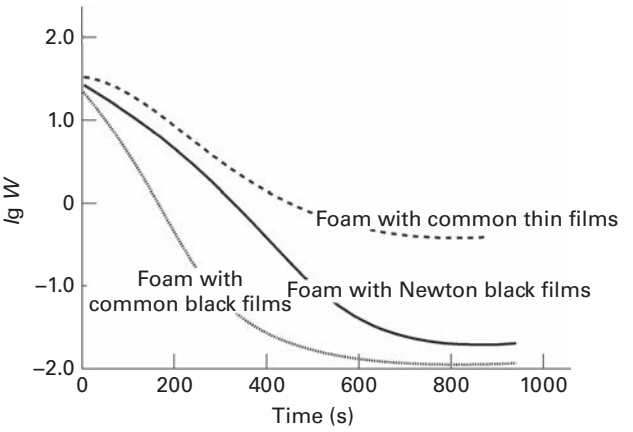

Fig. 4.17 Dependence of the water content W_l on the time t which is a measure of drainage at $\Delta P = 5 \times 10^3$ Pa for foams with different types of thin films: CTF, NBF films and CBF. From ref (21).

4.4 Disproportionation (Ostwald ripening)

The pressure inside the bubbles can be expressed by the Young–Laplace equation which defines the pressure over a curved surface (the capillary pressure). Upon shaking or stirring, an aqueous surfactant solution with a wide range of bubble sizes is initially generated, but, owing to the higher pressure inside the smaller bubbles compared to the larger ones coupled with the increase in gas solubility in the aqueous phase with pressure, gas tends to diffuse from the smaller bubbles to the larger ones via the liquid phase. This causes the transport of gas, leading to the growth of large bubbles at the expense of the smaller ones (which are shrinking) as illustrated in Fig. 4.18.

It can also be noted that the process is self-accelerating because as the larger bubbles grow in size and the smaller bubbles shrink, an increase in size discrepancy between the larger and smaller bubbles results, causing an increase in the driving force for gas diffusion from the smaller bubbles to the larger ones. Although, this kinetic diffusion generates a redistribution in bubble sizes, it does not necessarily result in a breakdown of the foam, since this can only be achieved by film rupture. However, detailed analysis of the disproportionation process gives valuable information on the stability of the system. It can also be noted that disproportionation occurs to a lesser extent in well-drained polyhedral foams (detergent foams with low liquid fraction <0.05) since in this case the lamellae are almost planar and there is no great pressure difference across the interface. However, with large bubbles stabilized by thick cell walls (protein foams), diffusion occurs remarkably rapidly near the top of the foam column and across the upper cell walls as the lamellae are highly convex, as shown in Fig. 4.19.

The mechanism of diffusive disproportionation in foams has been discussed in considerable detail in the earlier literature by Kitchener (22) and Prins (23). More recently, Farajzadeh and coworkers (24) in 2011 reviewed both the theoretical and experimental aspects of foam film permeability. In one of the early experimental studies in 1958,

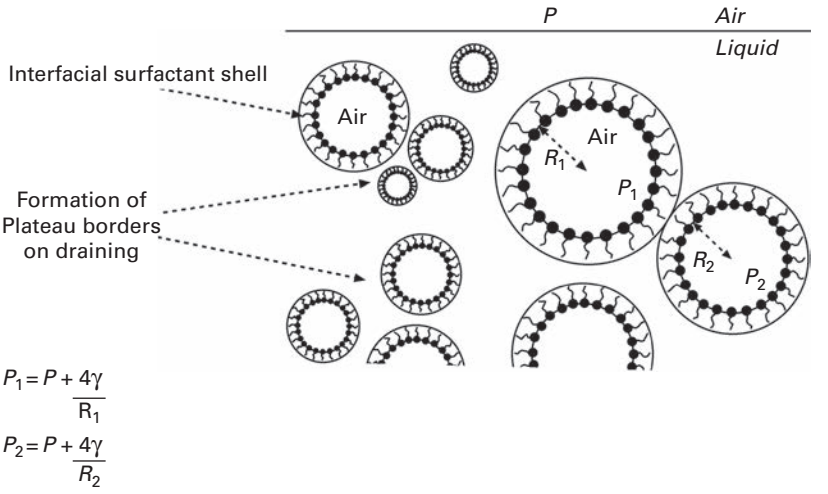

Fig. 4.18 Gas diffusion across foam (the continuous aqueous film and two films of the encapsulating surfactant shell). For gas diffusion $P_2 > P_1$ and $\Delta P = 4\gamma\,(1/R_2 - 1/R_1)$. The important parameters to consider during disproportionation are (a) the surface tension of the aqueous solution, (b) the bubble radii R_2 and R_1 and (c) the permeability of the surfactant film.

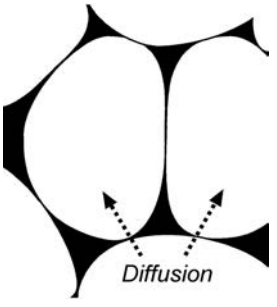

Fig. 4.19 Convex liquid interfaces inducing a diffusion effect across the thin film.

De Vries (25) derived a simplified equation based on the ideal gas law and Fick's first law of diffusion, which enables the approximate speed of the bubble shrinking process to be calculated. By assuming diffusive transport of gas from small bubbles to large bubbles at a separation distance (h_{sd}), the shrinking process was expressed as

$$R_t^2 = R_0^2 - (4RT\ D_g S_0 \gamma / P\ h_{sd})\ t \tag{4.12}$$

where t is the transport time, R_t is the shrinking bubble radius at time, t and R_0 are the bubble radius at $t = 0$, P is the atmospheric pressure, D_g is the diffusion coefficient of the gas in the liquid and S_0 is the gas solubility in the liquid. According to this equation, the bubble will shrink more rapidly in lower surface tension solutions and in cases where the solubility of the gas is high. From this equation, the changes in radii with time

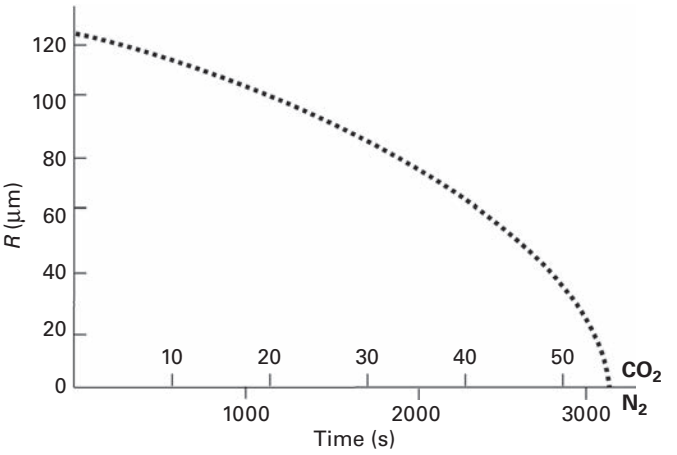

Fig. 4.20 Theoretical rates of disproportionation for CO_2 and N_2 at 20° C and 1 Atmosphere. The bubble radius R is plotted as a function of time t. The following values were chosen in the calculation: surface tension = 39 mNm^{-1}, R_0 = 125 μm, λ = 10 μm, D_g (CO_2) = 1.77×10^{-9} m^2/s and D_g (N_2) = 1.99×10^{-9} m^2/s, S_0 (CO_2) = 3.9×10^{-4} mol N^{-1} m^{-1} and S_0 (N^2) = 6.9×10^{-4} mol/N/m^{-1}. From ref (26).

for bubbles can be estimated for different gases. An example is shown for N_2 and CO_2 in Fig. 4.20.

These plots indicate that 40-μm-radii bubbles of CO_2 (which has a much greater solubility than N_2) have a lifetime of about 35 seconds, while for N_2 the lifetime is considerably longer (about 2000 seconds). However, the situation is more complex since the simplified equations assume that there is no resistance from the surfactant shell and the surface tension of the shrinking bubble is constant. In fact, values of the surface tension and surface elasticity of shrinking bubbles are lower than the equilibrium values, and recent studies by Georgieva and coworkers (27) indicate a dependency of the disproportionation process on the dynamic surface tension. In most theoretical models, it was more or less assumed that the surface tension remains constant.

4.4.1 Experimental methods with foams

Disproportionation experiments are difficult to perform on foams since disproportionation and drainage often occur simultaneously. To prevent this occurring, it is therefore essential to design experiments in which (a) the liquid fraction remains constant over long periods of time and (b) significant bubble size variations occur that can be accurately measured. Several different approaches have been made; one such example has shown it is possible to create foams under steady-state conditions by continuously bubbling gas, but this is difficult to achieve. An alternative technique is to rotate a cell which contains the foam. Figure 4.21 shows results from one of these studies (18) where the bubble sizes (as expressed by the relative variation of the PB length L_{PB} which is

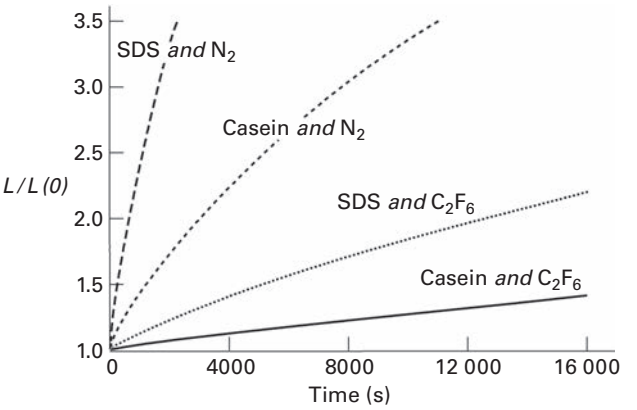

Fig. 4.21 Disproportionation data at constant liquid fraction. $L(t)/L(t = 0)$ for foams stabilized by SDS and casein with two different gases N_2 and C_2F_6 For each system the data can be fitted to extract a disproportionation time. From ref (18).

proportionate to the bubble diameter) are plotted versus time. The values of L were experimentally determined by light transmission, and throughout the experiments the liquid fraction remained constant at a value of 0.15. Two different gases (N_2 and C_2F_6) were used in the experiments, and the foams were stabilized with SDS and casein.

These curves were found to be consistent with the scaling $L \sim t^{1/2}$ at longer time periods. From the data a disproportionation rate constant and, hence, the effective diffusion coefficient (D_{eff}) was calculated. It can first be noted from these results for both surfactant systems that the increase in bubble size is considerably less for C_2F_6 than for N_2, which can be explained by the fact that C_2F_6 has an extremely low solubility in the aqueous phase. The surfactant type also plays an important role; casein stabilized foams grow about five to seven times slower than SDS foams from the initial bubble diameter (with the same gas and the same liquid fraction). At first sight, it would appear that this difference is due to differences in surface tension, but the thin film thicknesses of the adsorbed surfactants need also to be taken into consideration. It is well known from microscopic film studies that casein film coatings are about five to seven times thicker than SDS films, and the surfactant film thickness probably plays the most important role in the diffusion process.

4.4.2 Experimental methods with thin films

Due to the difficulties in performing experiments with dynamic foam systems, most studies have been carried out with thin liquid films. The most widely used technique is commonly referred to as the "diminishing bubble method" which is based on measurements carried out on an isolated thin film prepared between a bubble and the air/water interface. Essentially, a small bubble (radius about 100 μm) is released from an orifice in

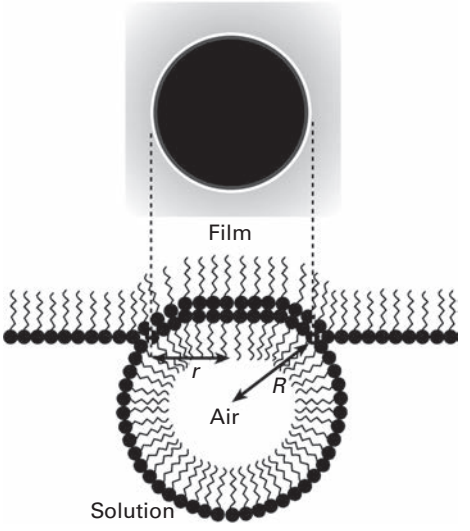

Fig. 4.22 "Diminishing bubble" method showing a bubble attached to the solution interface. The top image shows the bubble film that is observed through a microscope. *R* and *r* are the radii of the bubble and film, respectively. The diameter of the film is about 50 μm. From ref (28).

the base of a glass cell containing the surfactant solution. This bubble ascends to the interface, producing a thin film which is observed from below using a reflecting microscope. The foam film is also observed from the top of the bubble with a second microscope and the radii measured (Fig. 4.22).

Since the pressure inside bubble is higher than the outer pressure due to the capillary effect, gas diffuses across the thin film, shrinking the bubble, and the two radii decrease with time. The diffusion (permeability) coefficient is calculated from an established equation which relates values of the two radii at the start and end of the experiments. The first detailed experimental measurements with isolated films were reported by Brown and coworkers (29) in 1953, where a spherical bubble was assumed in the theory. Later Princen and coworkers (30, 31), in the 1960s, refined the method by analyzing the shape of bubbles, which enabled more precise data to be obtained. Other methods have also been developed based on trains of bubbles in glass tubes as well as layers of single foam bubbles. Princen and coworkers (31) also performed measurement on diffusion of gas through foam layers which were stabilized with soluble monolayers. From these types of studies, the influence of the surfactant, salt and temperature on the diffusivity were studied, and it has been generally concluded that Fick's law was reasonably applicable to macroscopic thick film systems. However, this simple diffusion model was found inadequate for Newton thin films (NFTs) constructed from surfactant bilayers.

4.4.3 Models and theories

Early theoretical models assumed that the bubbles were encapsulated by a homogeneous film of surfactant and water and that gas diffusing from one bubble to the next traverses

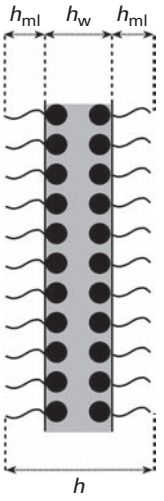

Fig. 4.23 A single-foam film consists of an aqueous core with thickness h_w sandwiched between two adsorbed monolayers of surfactant of $h_{ml.}$ The liquid and monolayers are assumed to be homogeneous.

through two shells consisting of the encapsulating aqueous film of lamella (the continuous phase). However, later it was recognized later that it was important to take into account the complex non-homogeneous structure of the shell when evaluating the diffusion rate. The model for this system is shown in Fig. 4.23.

From experimental studies, it has been established that gas diffusion occurred more readily in foams with simple monolayer surfactant films, rather than in foams stabilized by thick elastic crystalline gel-phase (produced by protein, polymer films or hydrophilic solid particles) or densely condensed surfactant phases. Experiments have been reported with many types of different surfactant systems, and it has been shown that films produced with ionic surfactants have a higher permeability than with non-ionic surfactants. In addition, both the size of the hydrophobic and hydrophilic segments and the geometry of the overall molecule were found to play an important role. The influence of the nature and concentration of electrolyte in the solution has also been documented because this can have a dual effect on the film structure. Primarily, electrolyte can increase the adsorption density of the surfactant (for an ionic) by screening the electrostatic interactions, producing a more compact layer, and it can also suppress the repulsive double-layer component of the disjoining pressure causing the film thickness to decrease. In an attempt to explain the wide range of experimental data, a considerable amount of work was invested in developing several sophisticated models. Some of these models and theories will be discussed in some detail in the following sections.

4.4.3.1 Diffusion theory

In the early studies by Princen and coworkers (30), a diffusivity coefficient (K_m of monatomic and diatomic gases) was related to the rate of gas molecules (dN/dt) passing through a liquid film of area A^f by the equation:

$$K_m = -1/A^f \Delta c_g (dN/dt) \tag{4.13}$$

$$dN/dt = -K_m A^f \Delta c_g \tag{4.14}$$

where Δc_g is the difference between the concentration of gas on either side of the film and K_m is considered to be the diffusive permeability of the surface monolayer. However, later it was found that this simplified approach based on Fick's law was to some extent unsatisfactory in explaining changes in diffusive behavior that occur with different types of surfactant molecules (with differences in chain length and hydrophobicity) which constitute the outer film barrier. In fact, in some cases, it was found to be more suitable to describe the process as a permeability rather than a diffusivity process, and the gas permeability coefficient k_f (cm/s) was introduced as a alternative of K_m.

Following this early approach, the model was modified to separate the enclosed aqueous core (with thickness h_w) from the two adsorbed monolayers of surfactants thickness h_{ml}. This approach enabled the k_f to be treated in terms of the thickness of the aqueous core as well as the solubility and diffusion of the gas through the monolayer coatings. The total film k_f was calculated from the equation

$$k_f = D_w H/(h_w + 2D_w/k_{ml}) \tag{4.15}$$

where D_w is the diffusion coefficient of gas in the aqueous core of the film, H is the Ostwald coefficient of the solubility of the gas in the aqueous solution, k_{ml} is the diffusion coefficient of a single surfactant monolayer and h_w is the thickness of the aqueous core. On increasing or decreasing the total film thickness, the thickness of the aqueous core changes, whereas the monolayer thickness remains constant. For thick films, the film aqueous core thickness $h_w >> 2D_w/k_{ml}$ and the diffusivity is characterized by the transport properties of the gas through the aqueous core. For $h_w < 2D_w/k_{ml}$, k_f is governed by the diffusivity of the adsorbed monolayer (k_{ml}). From early studies carried out on the effect of surfactant concentration, salt and temperature, it was concluded that this modified Fick's law model was satisfactory for macroscopic thick film systems with soluble monolayers. However, doubts have been raised concerning the validity of using Fick's diffusion theory in interpreting data in which the gas molecule is comparable in size to the thickness of the barrier (in the case of NBFs).

4.4.3.2 Energy barriers (nucleation theory and fluctuation of holes)

Alternative theories to Fick's diffusion were proposed where k_f was expressed in terms of an activation energy barrier, and it was assumed that each gas molecule required a precisely defined quantity of energy which was sufficient to pass through the space in the barrier. The magnitude of the energy barrier needed for transport was defined by the film structure and was dependent on such factors as the surfactant chain length, the cross-section area of the adsorbed phase, the state of compressibility of the film, the type of polar head groups, etc. Later, fluctuations and accessible surface area theories evolved where the permeability was considered to be dependent on the probability of the molecule approaching a hole in the surfactant layer and of

being of sufficient size to pass. Diffusivity (permeability) theories based on nucleation and hole formation were derived in which the coefficient of monolayer permeability (k_{ml}) was expressed in terms of the resistance of the monolayer to the penetration of gas molecules. Archer and La Mer (32) measured the rate of evaporation of water molecules through fatty acid monolayers and confirmed the existence of the energy barrier and defined k_{ml} in terms of an activation energy according to the equation

$$k_{ml} = B_4 \alpha_c \exp(E_a/R_g T) \tag{4.16}$$

where E_a is the activation energy, R_g is the gas constant, T is the absolute temperature, α_c is the condensation coefficient that accounts for the condensation on a monolayer free surface and B_4 is a constant that depends on the cross-sectional area of the gas.

The Nucleation Theory of Fluctuations explains the formation of holes in bilayer and proved useful in explaining the permeability through NBFs. Essentially, it is based on the assumption that defects are present in the adsorbed monolayer. The existence of holes or gaps in films was explained by the imperfect arrangements of the molecular structure within the film, and permeation could only occur when the molecule approaches a hole with a critical size. It was proposed there were two distinct regions in the foam bilayer: (a) a hole-free area with a permeability k_0 (coefficient of background permeability) and (b) areas that consist of holes of different sizes.

4.4.3.3 Freely standing film

A "free film standing diffusion model" (33) was also developed in 2002 to investigate the resistance of one or more films to the mass transport of gas molecules through a foam. This was extended on a matrix structure (consisting of a train of foam films) as shown in Fig. 4.24. In this theory effective gas diffusivity was related to the foam film density (the number of foam films per unit of length of the matrix). In the presence of n_f intervening foam films (each with equal thickness of h_f), the one-dimensional gas space was divided into ($n_f + 1$) sections as illustrated. The whole system is assumed to have an effective diffusion constant D_{eff} and the gas flux is reduced as a result of the film resistance $1/k_{eff}$, with k_{eff} being the effective coefficient of the gas transfer across n_f films. This model also was found to be satisfactory in explaining the changes in diffusion caused by changes in surfactant concentration and the length of hydrocarbon chain as well as temperature and electrolyte.

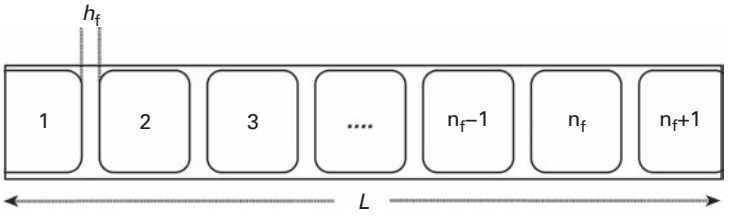

Fig. 4.24 Schematic of a train of foam films with equal thickness of h_f in cylinder with length L. In the presence of intervening foam films, the gas space is separated into $n_f + 1$ sections. From ref (40).

4.4.3.4 Density fluctuations and accessible areas

The "accessible area theory" is also based on the probability of gas molecules finding a gap in the film, but, in this case, the sum of the areas of available holes (which are formed spontaneously at the surface) was taken into consideration. In this approach, it was proposed that the probability of finding holes (free spaces in the surfactant monolayer) depends on (a) the natural free area in the lattice and (b) the local fluctuations occurring in the monolayer. The kinetic energy of the gas molecule was also taken into consideration, and it was assumed that this must be of sufficient magnitude to force the monolayer molecules apart. Generally, reasonable descriptions for permeability have been established when considering the equilibrium properties of a monolayer, but this approach has been found to be less effective when considering monolayer dynamics.

4.4.4 Experimental results

Measurements of the permeability of thin foam films to gas molecules enable many of these theories to be tested, and important information on the structure and intermolecular interactions in the adsorbed layers has been established. For NBFs, high concentrations of electrolyte are required to produce the structures, the surfactant monolayers are very close and are in a condensed state separated by only a few water layers, and the permeability value is fairly high. In this case, the Derjaguin, Landau, Verwey, Overbeek (DLVO) theory often cannot account for stability due to surface density fluctuations as discussed in Chapter 3. CTF and CBF have a sandwich structure, with two monolayers of adsorbed surfactant in a less dense state separated by an aqueous core. Such structures are usually formed in a weak electrolyte with the stability behavior following DLVO theory. At higher surfactant concentrations (above the CMC), micelles may be present in the aqueous core and can act as a reservoir for releasing monomers of surfactant which may adsorb at the interface during changes in thickness or pressure. In this case, the permeability is considerably lower. Figure 4.25 illustrates the structure of different types of films.

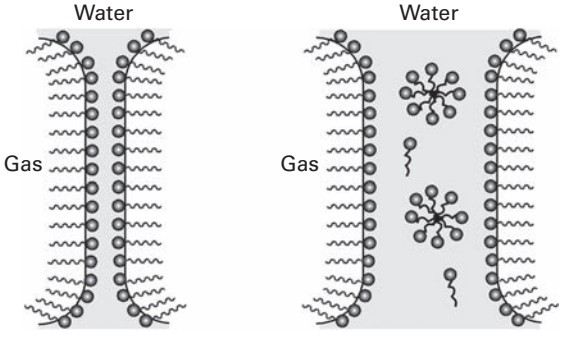

Fig. 4.25 Two equilibrium states of a foam film: (a) an NBF has a dense bilayer structure with the monolayers separated by only an inner core containing only a few layers of water; and (b) a CBF with a thicker central aqueous core with two monolayers of adsorbed surfactant. Micelles act as a reservoir, releasing monomers of surfactant which may adsorb at the interface during changes in thickness or pressure. The addition of fairly high concentrations of electrolyte leads to the formation of CBFs.

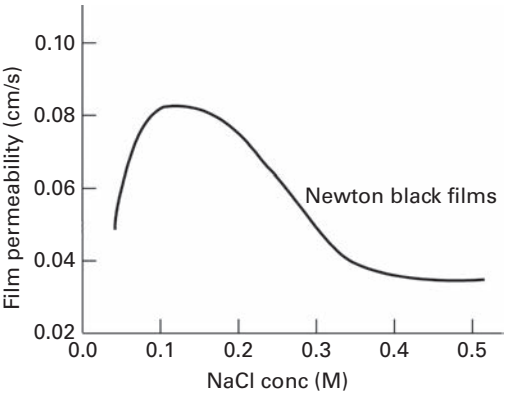

Fig. 4.26 Permeability versus NaCl concentration for foam films stabilized by AOS. The results for the different AOS concentrations (3×10^{-4} M and 9.5×10^{-3} M) fit the same curve. At high NaCl concentrations, NBFs predominate. From ref (35).

Gas permeability measurements are usually carried out with purified surfactants under precisely defined conditions at different concentrations and at constant ionic strength or at constant surfactant concentration and variable ionic strength. The presence of a critical amount of electrolyte assures the formation of CBFs and NBFs. In 2009, Farajzadeh and coworkers (34) determined that the gas permeability of NBFs stabilized by alpha-olefin sulfonate (AOS) at two different surfactant concentrations (3×10^{-4} M and 9.5×10^{-3} M) at a range of electrolyte concentrations temperatures. In Fig. 4.26, the values of the permeability coefficient at increasing NaCl concentration for the two different AOS concentrations and shown with a single curve fitting both sets of data. Interestingly, the change in AOS concentration did not influence the results at both concentrations, and the film permeability was found to increase with the increase in electrolyte concentration within the low NaCl concentration regions (where a decrease in the film thickness must occur due to a reduction in double layer potential).

However, this only occurred up to a critical permeability value; beyond this, it corresponded to a region of NBF formation, where it was found to decrease even though the film thickness decreased. These results were difficult to explain; however, they were discussed in terms of a sandwich model that suggested that the changes in permeability were due to a balance between the permeability of the adsorbed monolayer that increased in permeability (but not in thickness) as the electrolyte concentration increased. This was explained by an increased in adsorption density, whereas the permeability of the water film remained fairly constant, but the thickness decreased on increasing the NaCl concentration. At high NaCl concentration, NBFs predominate, and several researchers have suggested that the transition from CBF to NBF (which involves a molecular rearrangement and a possible phase change) can cause an increase in the strength of the molecular interaction between the two monolayers, and this can also result in an additional increase in adsorption density, causing a decrease in film permeability.

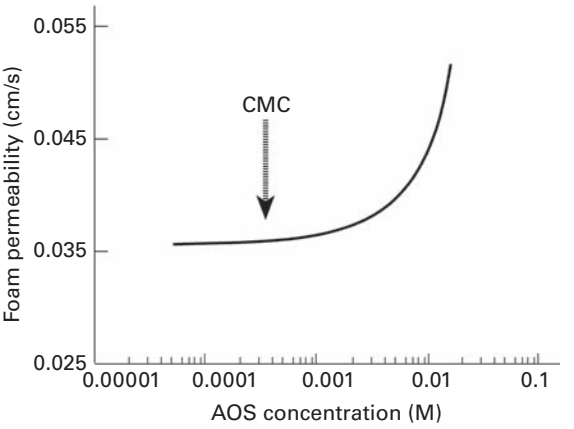

Fig. 4.27 Permeability versus AOS concentration at constant NaCl concentration (0.5 M) at 24°C. Under these conditions only NBFs are formed. The CMC is at 1.3×10^{-4} M AOS. From ref (34).

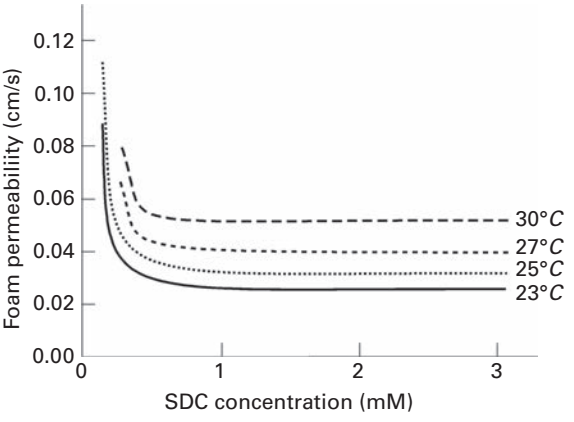

Fig. 4.28 Permeability versus surfactant concentration at four temperatures for films prepared from SDS solution containing 0.5 M NaCl. From ref (36).

It was also reported that upon increasing the surfactant concentration at high salt (0.5 M NaCl), the permeability shows a dramatic increase at concentrations above 10^{-4} M AOS, as shown in Fig. 4.27. However, this behavior again could not be fully explained, although it may be associated with the structural changes in the NBFs.

Gas permeability data were also measured at different temperatures, which enabled the energy barrier of the process to be estimated. An interesting series of experiments on NBFs were carried out with SDS surfactant in aqueous NaCl (0.5 M) at four different temperatures over a wide surfactant concentration range, and the results are shown in Fig. 4.28. In this plot, the value of gas permeability was found to remain fairly constant in the higher concentration SDS range (1–3 mM), but in the lower SDS concentration regions the value increased with decrease in SDS concentrations. Overall, permeability

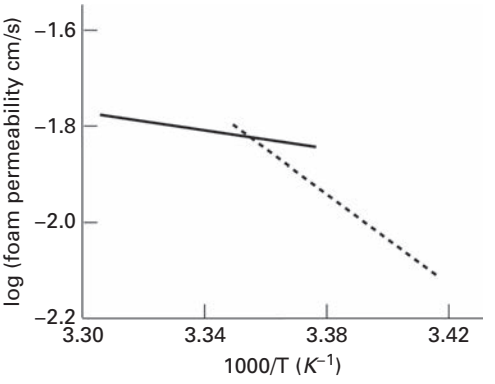

Fig. 4.29 Gas permeability versus temperature in Arrhenius coordinates for CBF from 1.73 mM SDS + 0.5 M LiCl aqueous solution. From ref (37).

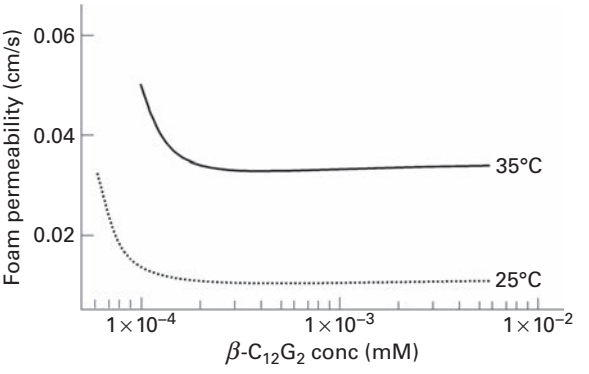

Fig. 4.30 Permeability versus concentration of beta-$C_{12}G_2$ concentration at two different temperatures and at a constant electrolyte concentration (0.2 M NaCl). From ref (31).

increased with the increase in temperature, and from the temperature data Arrhenius plots were constructed (Fig. 4.29). The changes in slope within certain temperature ranges were used as evidence for changes in the mechanism of gas permeability in NBFs.

It has also been suggested that pronounced transitions in permeability were influenced by the CMC of the surfactant, but this concept is in need of verification. In most of the experimental studies on NBFs, the data were treated using the nucleation theory of fluctuation formation of holes in bilayer and free-standing film theory, and sometimes it was found possible to fit both theories to the data. Interestingly, data relating the permeability to surfactant concentration of nonionic sugar-based surfactants, *n*-dodecyl-β –D-maltoside (β -$C_{12}G_2$), at two different temperatures was obtained by Muruganathan and coworkers (38) (Fig. 4.30). These results indicated that the permeability initially decreases with increase in concentration and also increases with temperature, which verified the experiments with SDS where the theory of nucleation was found to be applicable.

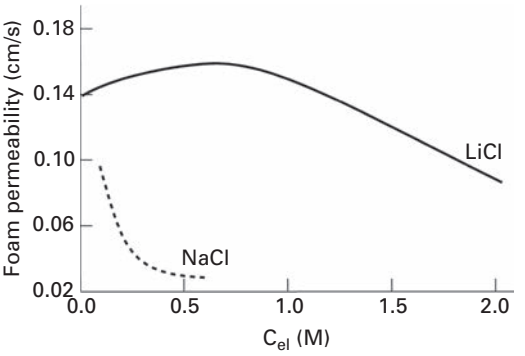

Fig. 4.31 Permeability versus electrolyte concentration (Na and C_s) for C_{sds} = 1.73 mM and at 24°C. From ref (35).

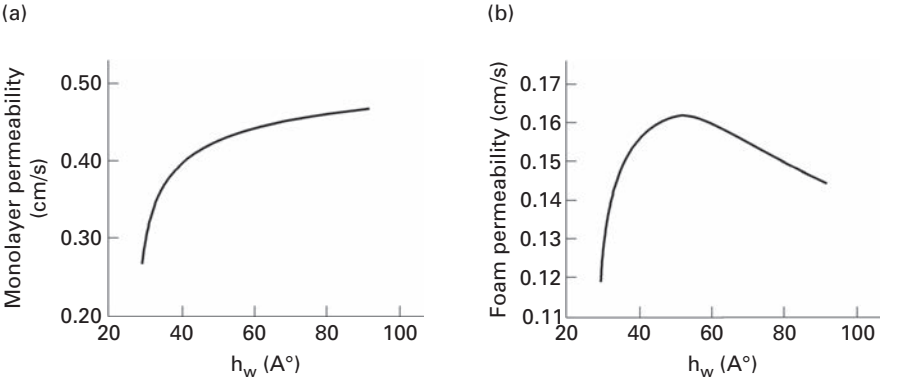

Fig. 4.32 (a) Dependence of the monolayer permeability on the thickness of the inner aqueous layer of CBF stabilized by SDS and LiCl solutions and (b) dependence of the film permeability on the thickness of the inner aqueous layer of CBF stabilized by SDS and LiCl solutions. From ref (37).

It has also been established that the type of inorganic electrolyte which is used to define the ionic strength of these systems also has an influence on the permeability. The results obtained by Krustev and coworkers (35, 37) for the permeability of foam films stabilized with SDS surfactant with electrolytes of different cations (NaCl and LiCl) at a range of concentrations is shown in Fig. 4.31, together with the corresponding changes in film thicknesses (Fig. 4.32).

It appears that the transitions in permeability in the SDS/NaCl system are more pronounced than with SDS/LiCl where the permeability decreases more gradually and transitions becomes less clear. These results may be explained by difference in the specific adsorption characteristics of the cations at the film interface. It was suggested that the smaller Na^+ was more strongly adsorbed at the SDS monolayer which resulted in increased compaction and a more structured ordering, decreasing the permeability compared to the Li^+. Farajzadeh and coworkers (34) showed not only that it was possible to fit the experimental data of the monolayer permeability of the films to the "accessible

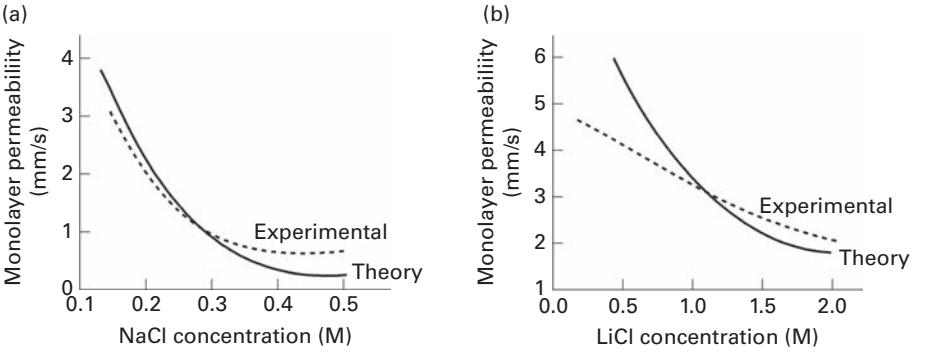

Fig. 4.33 Permeability of the monolayer versus electrolyte concentration. Experimental and theoretical curves are shown based on ECI theory estimated by applying accessible area theory for gas permeation and ECI (Enhanced colloidal interactions) theory for the surfactant adsorption density on the film surface. From ref (39).

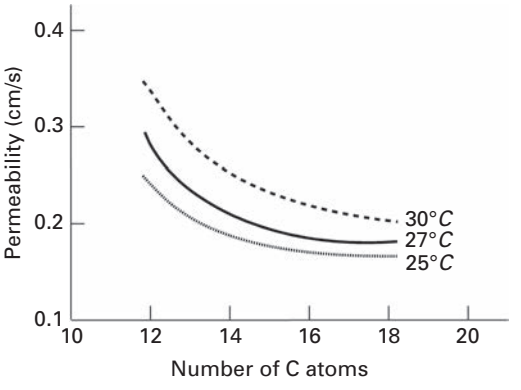

Fig. 4.34 Permeability versus carbon atoms in the alkyl chain for alkyltrimethylammonium for NBFs at three different temperatures. From ref (40).

area theory," but also that it was possible to explain the data in terms of an enhancement of interactions caused by changes of interfacial excess quantities mediated by long-range forces, as indicated by Muller (39) (see Fig. 4.33).

It has also been confirmed that the permeability of the foam film decreases with increase in alkyl chain length for experiments carried out with a cationic surfactant (Fig. 4.34), and this behavior was explained from the energy barrier theory. A film containing a higher hydrocarbon chain length would be more compacted and more difficult to penetrate by gas molecules compared to a film constructed from shorter hydrocarbon chain length molecules. At higher temperature, permeability increases, thus confirming earlier experiments.

For a homogeneous series of ethoxylated nonionic surfactants ($C_{12}E_n$), it was reported that permeability decreases with increasing head group size (41) (Fig. 4.35).

However, since the thickness of the NBF decreased with a decrease in the size of the hydrophilic head group (number of EO chains), this could explain the decrease in

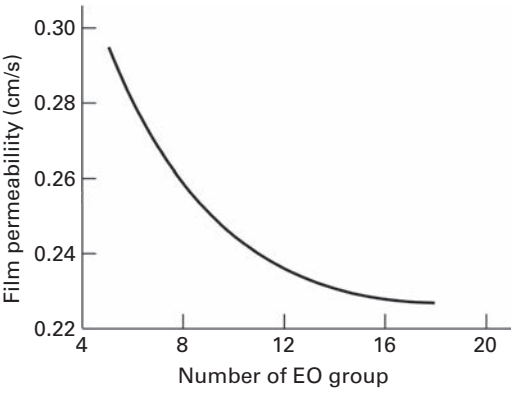

Fig. 4.35 Permeability versus number of EO groups in chain of $C_{12}EO_n$-type surfactants for foam films. C_{surf} = 2 CMC and C_{NaCl} = 0.1 M at 22°C. From ref (41).

permeability. It is also important to take into account the flexibility of the coil structure of the EO which influences both packing and film thickness (41). In addition, larger head group ethoxylated molecules can form gel phases inside the core which are difficult for the gas to penetrate. It was also reported that the gas permeability of thin liquid films stabilized by a polymer (*N*-isopropylacrylamide) was mainly determined by the structure of the adsorbed polymer layer and this would probably produce an effective gas permeability coefficient comparable to that of an NBF produced from SDS surfactant. However, on adding SDS to the polymer the permeability coefficient of the co-adsorbed polymer/surfactant mixture increased, indicating an increase in porosity of the mixed film.

Overall, from these studies it can be concluded that the CBFs have higher permeability than NBFs, which is, in the case of the thin NBFs, determined by the adsorbed outer layers (monolayers) rather than the inner core of the bilayers. As the thickness of the inner core is reduced, the normal cohesive interactions between the monolayer molecules usually cause an increase in structural packing which decreases the permeability. The permeability of CBFs and NBFs for nonionic and cationic surfactants are fairly similar, and in this case the permeability is less sensitive to film thickness. However, the situation is complex since the nature of the gas also plays a role in the diffusion process. For all types of surfactants the gas permeability of the foam film was reported to be largely dependent on the solubility of gas in the surfactant solution and to increase with increasing solubility in the bulk solution.

4.5 Coupling disproportionation with drainage

In a typical foam, inter-bubble diffusion causes smaller bubbles to reduce in size and larger bubbles to enlarge with time; the liquid between the bubbles drains out and these two processes affect each other. This occurs particularly in wet foams

(high water content) where the bubbles are separated by thicker layers of liquid where only slow gas diffusion between bubbles occurs and the liquid drains slowly. As the drainage proceeds, the thickness of the liquid film between bubbles is reduced; this increases the disproportionation rate, which in turn further increases the drainage. Since drainage and disproportion are interdependent, Hilgenfeldt and coworkers (42) defined a K_H value in terms of the ratio of drainage time t_d and disproportionation time t_{dis}($K_{dc} = t_d/t_{dis}$) which could be expressed by the equation

$$K_H = \frac{4\eta_\ell H_f D_{eff} f(\Phi_\ell)}{K_n^o \rho_\ell g \Phi_\ell d_b^4} \tag{4.17}$$

where H_f is the foam height, d_b is the diameter it the bubble, K_n^o is the the dimensionless permeability, and D_{eff} is the effective diffusion coefficient that takes into consideration the dependence on the coarsening rate with liquid fraction (Φ_ℓ). This equation enables disproportionation and free draining to be treated simultaneously. For long t_{dis} values, the disproportionation can be neglected during drainage and the bubble size remains constant, but in the case of for short t_{dis} the bubble size varies during drainage and the dynamic of drainage is accelerated. Due to this coupling effect, the drainage time can be strongly reduced by disproportionation, and this combined effect is illustrated in Fig. 4.36 which shows drainage curves in which volume of liquid drained, normalized by the final volume of liquid drained, is plotted as a function of time. Two gases – N_2 and C_2F_6, which are sparsely soluble in the aqueous solution – were used in these studies and the foams were stabilized by SDS.

With foams generated under $N_{2(g)}$, disproportionation occurs during drainage and the resulting drainage time is higher than those formed using C_2F_6(g). In the extreme case of high disproportionation, it has been predicted and observed that the volume of drained liquid first follows a quadratic behavior. The dependence on the liquid content is also

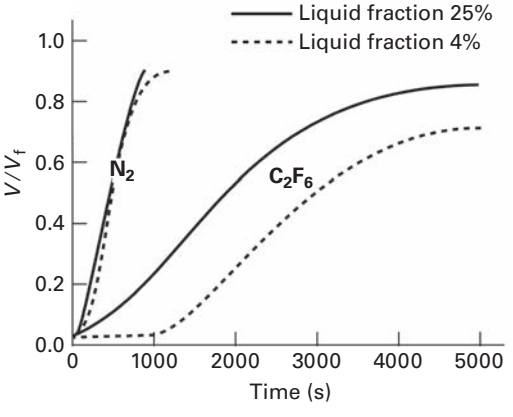

Fig. 4.36 Free drainage curves (relative velocity versus time) for dry (4% water content) and wet (25% water content) SDS foams generated by two different gases, N_2 and C_2F_6. The disproportionation proceeds simultaneously with drainage (N_2) and the drainage process is accelerated and variation with the liquid fractions vanishes. From ref (18).

expected to vanish, and a self-limiting drainage is observed. On the contrary, for C_2F_6 where the foam undergoes low disproportionation during drainage, there is no clear dependence of the drainage time on the liquid fraction. It is proposed from the study that strong disproportionation caused a pronounced acceleration effect of drainage which tended to reduce the foam lifetime.

Free drainage experiments were also carried out with a low soluble gas (C_2F_6 and a high soluble gas (CO_2), and different dynamics with the coupling of disproportionation to drainage were reported (42). Strong disproportionation led to shorter drainage time (accelerated drainage) which was independent of the initial liquid content. A model was developed incorporating the physics of drainage and diffusive disproportionation which was found to agree with the experimental data. The coupling between drainage and disproportionation was also studied by Saha and coworkers (43), using a Gilllette shaving foam in which the growth in bubble size was measured by direct imaging along the height in a foam column. Simultaneously, the drainage of liquid was investigated by Raman spectroscopic measurements. The data were fitted to an empirical relationship.

4.6 Depletion of surfactant from solution

The adsorption of surfactant at the air/water interface is essential for foaming, but at high flow rates this may cause a depletion of the surfactant in bulk solution. In 2012, Boos and coworkers (44) quantified depletion effects from experimental foaming studies carefully carried out in a commercially available Foam Scan Apparatus (45). This enabled foams to be generated at constant gas flows as a function of time; by adjusting the equipment, the final volume of the foam produced (V_{end}) could be pre-set and the stability and decay time could be evaluated. A measure of the depletion of surfactant from bulk solution was determined from surface tension measurements which were carried out at the end of the foam-generation step where the bulk surfactant solution was sampled by extraction from the Foam Scan column. In addition, the bubble size and distribution and the Sauter mean cell radii of the bubbles were also obtained from the Foam Scan cell analysis function. Using these data, the degree of surfactant depleted from solution was calculated using a theoretical model based on calculating the geometrical interface of the foam. In this study, two nonionic surfactants with similar CMC values but different foaming characteristics were tested, namely, *n*-dodecyl β-D-maltoside (β-C_{12} G_2), which produced a high-volume stable foam, and hexaethylglycol monododecyl ether ($C_{12}E_6$), which produced a low-volume unstable foam.

In the first series of experiments, different foam volumes were generated (which correspond to the V_{end}) with the same surfactant solution at a concentration of 2 × CMC, and it was found the higher the foam volume, the greater the amount of surfactant depleted from bulk solution. In a second series of experiments, foam was generated with (β-C_{12} G_2) at two different bulk concentrations of surfactant (c = 2 CMC and 1.33 CMC) to give two different foam volumes (50 ml and 110 ml). Figure 4.37 shows the bubble

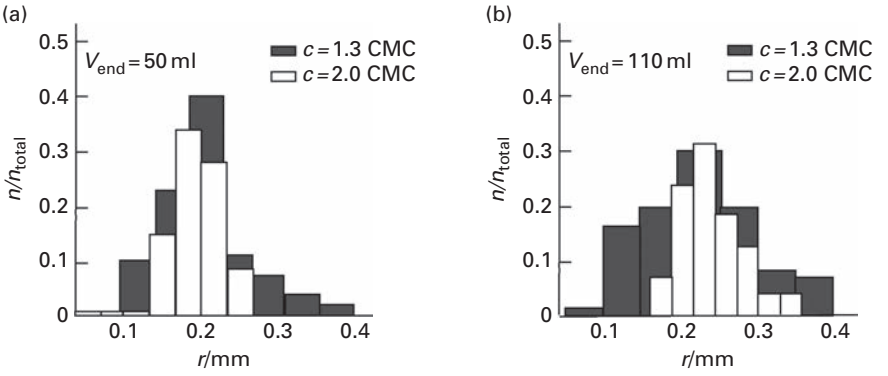

Fig. 4.37 Comparison of bubble size distribution from *n*-dodecyl *β*-D-maltoside (β-$C_{12}G_2$) at c = 1.33 CMC and c = 2 CMC calculation made using cell-size analysis software and image analysis of pictures taken at time t = 0 (time at which the pre-set foam volumes of V_{end} = 50 ml and 110 ml are reached). From ref (44).

size distributions of the foams versus the relative number of bubbles n/n_{total}, where n_{total} is the total number of bubbles in a foam.

Figure 4.37(a) compares the bubble size distributions obtained for two initial bulk concentration c = 2 CMC and 1.33 CMC at the lower pre-set foam volume (50 ml), and Fig. 4.37(b) compares them at the higher foam pre-set foam volume (110 ml). With foams of lower pre-set volume (50 ml), the two bubble size distribution appear fairly similar, indicating low depletion effects, whereas in the higher pre-set volume foam (110 ml) a wider size distribution was reported, suggesting a more pronounced depletion of surfactant at the lower surfactant concentration. This depletion effect was verified from surface tension data. From these studies it was also concluded that depletion is important in cases where large foam volumes are generated (which was as expected); however, it was noted that it occurred at surfactant concentrations above the CMC. In addition, good agreement between calculated (based on a simplified model) and measured depletion effects was established, and it could be suggested that the theoretical approach using cell-size analysis was an effective method for quantifying depletion effects.

4.7 Humidity and evaporation

The stability of foam is well known to be dependent on humidity and evaporation processes, and there have been early reports of bubble bursting at the surface of foam which appears to be caused by evaporation. Figure 4.38 shows the external film on the surface of the foam in an idealized 2D foam structure. For a foam in equilibrium, this initial rupture step can lead to an avalanche effect spreading downward through a foam column, but in a dynamic column fresh bubbles reaching the interface will retain the stability.

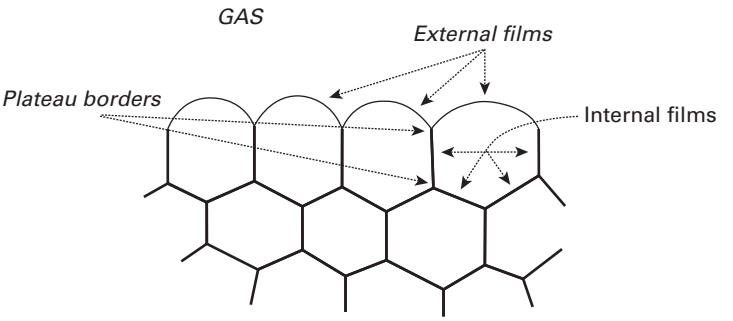

Fig. 4.38 2D illustration of the initial rupture of the external film in an idealized foam structure. From ref (46).

Exowera and Kruglyakov (47) described early Russian studies in which foam stability was decreased by increases in evaporation rates. Tamura and coworkers (48) also reported that the stability of a single, free thin film decreases when the humidity of the surroundings is reduced. Also, it has been shown that saturating the air above the foam and preventing evaporation can retard foam collapse. In low relative humidity (RH) conditions, vigorous fluctuations occurred in the foam films while at high RH conditions (values of 60% and 75%) the films were remarkably stable. Systematic humidity-controlled foaming studies were also reported by Lu and coworkers (49) in 2010. In these experiments, a foam was generated with SDS (at concentrations about 25% greater than CMC) in a square-sided perspex chamber with a glass frit at the base of the column through which gas was sparged via a humidifier/buffer system. Measurements were made at the height of the space between the foam bed surface and the top of the column, and this distance was described as the freeboard height. Initially, the humidity of the top of the freeboard height was adjusted by introducing a stream of dry air via a valve below the top of the column, and the flow rates of both dry air and humidified air could be manipulated and monitored. A humidity sensor was fitted to a small vent at the top of the column. Throughout the experiments, the bubble size was estimated from photographs, and in the initial series of tests foaming was carried out at a range of constant superficial gas flow velocities with an RH of 40%. The results are shown in Fig. 4.39.

In these plots, it can be seen that the foam height increases approximately linearly with time at each value of the superficial gas flow velocity before leveling off, which was interpreted as the region where the rate of foam collapse almost balances the rate of generation of fresh foam. At increasing superficial gas flow velocity, a greater height of foam was generated. Usually, the foam height divided by the superficial gas velocity is used to quantify foam stability. In further experiments at the same surfactant concentration, the relative humidity (RH) at the top of the column was increased to 96%, and the result were compared with the case of the foaming at 40% humidity at the same gas flow rate. This showed that the foam height continued to grow linearly toward the top of the column under the higher humidity conditions as illustrated in Fig. 4.40. Then the concentration of SDS was reduced by 90% (to ~1 mM) to give a concentration well below the CMC, and tests were carried out at 40% and 90% RH. The results, showing higher humidity sample

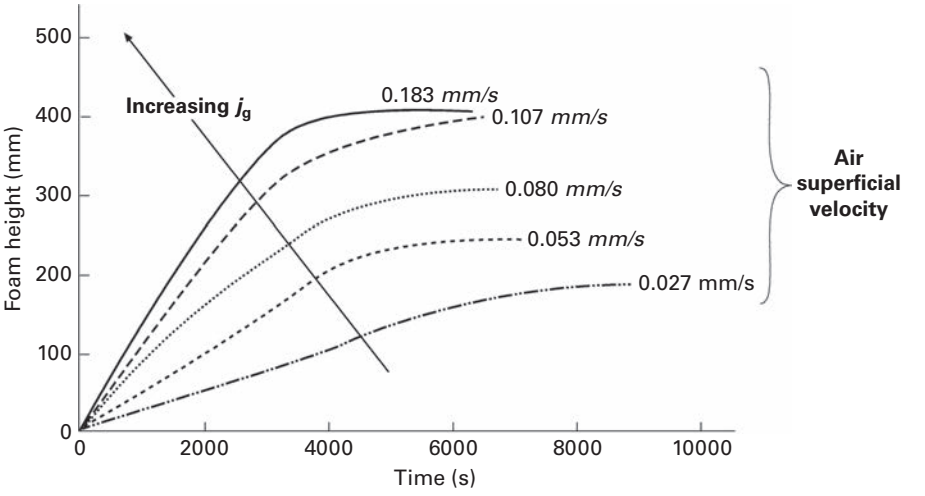

Fig. 4.39 Foam growth at different values of the air superficial velocities (j_g). The relative humidity at the top of the column was 40%. The foam was generated from a solution of SDS (~10 mM). From ref (49).

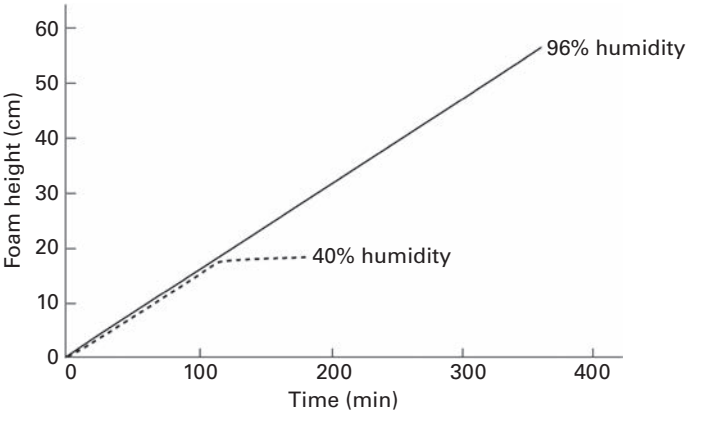

Fig. 4.40 Foam growth at air superficial velocities of 0.027 mm/s. The relative humidity at the top of the column was 40% and 96%. The foam was generated from a solution of SDS (~10 mM). From ref (49).

growing to a higher value compared to the lower RH sample. This indicated that these RH effects were also important in dilute surfactant solution.

Experiments were also carried out at an RH set at 40% and the SDS concentration at ~10 mM, but in this case the height above the column was increased by extending the tube (increasing the freeboard height) from 0.9 to 1.2 m; the results are shown in Fig. 4.41. These results show that on increasing the height of the space above the foam column, a more stable foam could be generated, suggesting that it was not the absolute value of relative humidity directly at the top of the column that influenced the foam stability, but that it was more dependent on the relative humidity changes in the

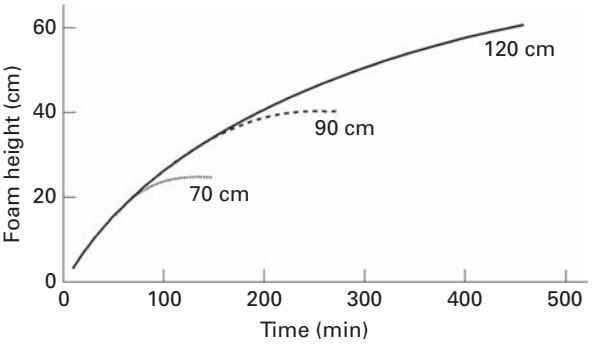

Fig. 4.41 Foam growth at different values of the total column height (distance between liquid foam interface and the top of the column shown in legend). Relative humidity 40% and the foam generated by SDS solution (~10 mM). The superficial gas flow velocity was 0.053 mm/s. From ref (49).

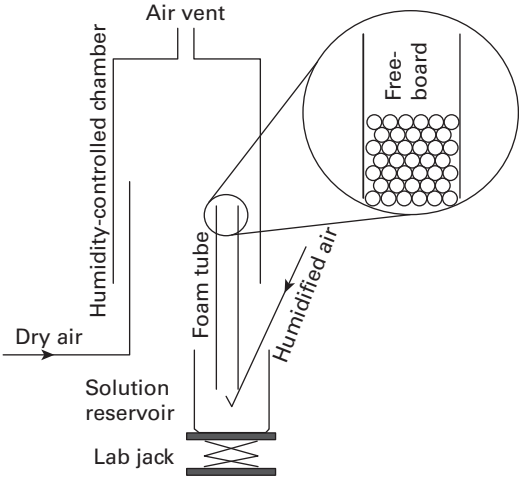

Fig. 4.42 Schematic diagram of the humidity-controlled foam stability apparatus. From ref (50).

freeboard region. In fact, the humidity gradient was probably the driving force for evaporation, and this increased as the freeboard height increased.

Overall, it was concluded from these experiments that foam height can be controlled by regulating the humidity gradient that governed the evaporation rate from the foam surface. These concepts were verified by Li and coworkers (50) who developed a more refined foam stability/humidity test apparatus (Fig. 4.42) in which foams are created in tubes and their collapse monitored under controlled RH environment.

With this equipment, the length of the foam tube and the humidity gradient (the freeboard height) could be adjusted and the collapse process could be monitored by a computer-controlled camera. In this study, cetyl ammonium bromide (CTAB) was used at a concentration of 0.5 g/l as the foaming agent (since this surfactant is known to be less sensitive to temperature), and static foams were generated with controlled

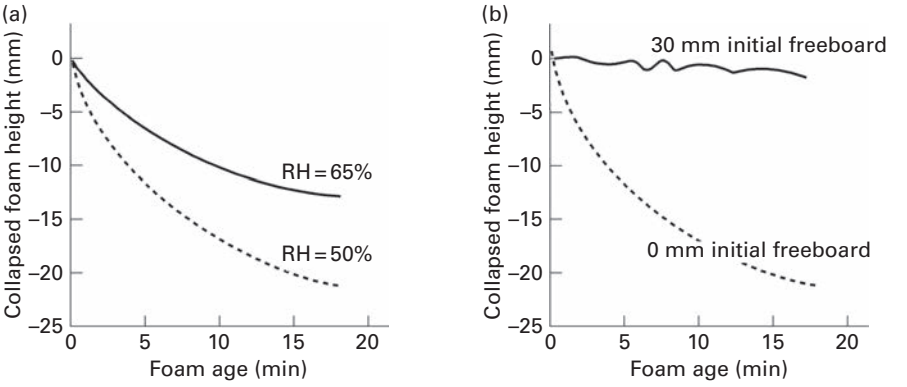

Fig. 4.43 Collapse foam height versus age of foams generated from CTAB (0.5 g/l) (a) with two different relative RH values at the same initial freeboard height ($t = 0$ mm) and (b) with two different initial freeboard heights but with the same RH = 50%. The bubble size, initial foam height and initial liquid fraction are identical in all cases. From ref (50).

bubble size and liquid fraction. Figure 4.43(a) shows the stability of the static foams generated under RH values of 50% and 65% at a freeboard height with zero value, and Fig. 4.43(b) shows the stability of foams with the same RH of 50% but different freeboard heights.

These results show that low-humidity foam is less stable under conditions where the foam has identical freeboard height (Fig. 4.43a), but in the case where foams are produced at the same RH value, the foams generated at lower freeboard height are less stable. The concept of humidity gradient (as a driving force for evaporation) which decreases as the freeboard height increases appears not to have been considered in the conventional understanding of foam collapse. Experiments have also shown that the RH can influence the dynamic surface tension, which could affect the rupture of isolated bubbles and the stability of thin foam films. Experiments were carried out under saturated and unsaturated vapor conditions using the pendant bubble method where a bubble was immersed in the solution and evaporation eliminated; this was compared with the pendant drop method where a drop is created at the tip of a needle.

The results shown in Fig. 4.44 indicate that at 100% RH during the evolution of drop volume, the drop volume remains constant with time but surface tension decreases as adsorption increases. At 45%, the drop volume decreases with time, but the surface tension also decreases slightly faster due to loss of water from the surface. These studies are important since they could have implications for froth stability in mineral processing where flotation plants frequently operate throughout a wide range of seasonal RH values.

A hypothesis for bubble bursting was proposed involving Marangoni instability induced by non-uniform evaporation, which could help to explain the dependency of foam stability on RH. Direct observation of the bursting process of isolated bubbles by high-speed video recording and also thinning of isolated foam films under different values of humidity and temperature by micro-interferometric methods were made and gave some support to these ideas.

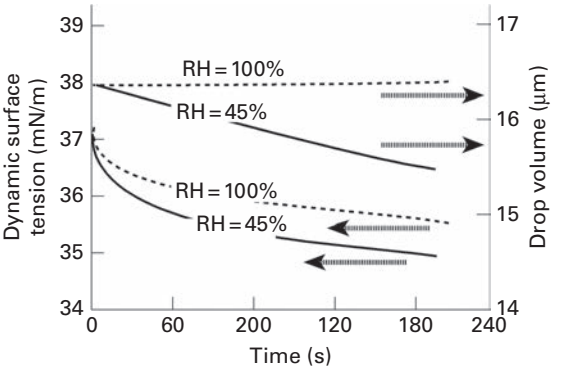

Fig. 4.44 Dynamic surface tension and drop volume at different relative humidities. From ref (50).

References

(1) W. Rybczynski, *Bulletin Int De L' Academie ds Sciences De Cracovie, Classe des Science Mathematiques et Naturelles Series A, Science Mathematiques*, Cracovie, Imprimerie de l' Universite, Janvier 1A, **40**, 1911.

(2) Hadamard-Rybczynski cited by S. S. Dukhin, G. Kretzsmar, R. Miller, *Dynamics of Adsorption at Liquid Interfaces, Theory, Experiments, Application*, Elsevier Publications, 1995.

(3) V. G. Levich, *Physicochemical Hydrodynamics*, Prentice-Hall, Englewood Cliffs, NJ, 1962.

(4) J. J. Bikerman, *Foams*, Springer-Verlag, Berlin, 1973.

(5) S. S. Dukhin, R. Miller and G. Logio, *Physic-Chemical Hydrodynamics of Rising Bubble in Drops and Bubbles Interfacial Research*, Ed. D. Mobius and R. Miller, Elsevier Publications, pp. 367–433, 1998.

(6) K. Malysa, M. Krasowska, M. Krzan, Influence of Surface Active Substances on Bubble Motion and Collision with Various Interfaces, *Adv. Colloid Interface Sci.*, **114**–**115**, 205–225, 2005.

(7) M. Krzan, K. Lunkenheimer and K. Malysa, On the Influence of the Surfactant's Polar Group on the Local and Terminal Velocities of Bubbles, *Colloids Surf., A*, **250**, 431–441, 2004.

(8) J. Zawala and K. Malysa, Influence of Impact Velocity and Size of the Film Formed on Bubble Coalescence Time at Water Surface, *Langmuir*, **27**, 2250–2257, 2011.

(9) M. Krzan, K. Lunkenheimer and K. Malysa, Pulsation and Bouncing of a Bubble Prior to Rupture and/or Foam Film Formation, *Langmuir*, **19**, 6586–6589, 2003.

(10) J. Zawala, K. Swiech and K. Malysa, A Simple Physicochemical Method for Detection of Organic Contamination in Water, *Colloids Surf., A*, **302**, 293–300, 2007.

(11) D. Weaire and S. Hutzler, *The Physics of Foams*, Clarendon Press, Oxford, 1999.

(12) R. A. Leonard and R. Lemlich, Laminar Longitudinal Flow between Close Packed Cylinders, *Chem. Eng. Sci.*, **20**, 790–791, 1965.

(13) S. A. Koehler, S. Hilgenfeldt and H. Stone, A Generalized View of Foam Drainage: Experiment and Theory, *Langmuir*, **16**, 6327–6341, 2000.
(14) A. Saint-Jalmes, Y. Zhang and D. Langevin, Quantitative Description of Foam Drainage: Transition with Surface Mobility, *Eur. Phys. J. E.*, **15**, 53, 2004.
(15) P. M. Kruglyakov, S. I. Elaneva, N. G. Vilkova and S. I. Karakashev, Investigations of Foam Drainage Using Foam Pressure Drop Technique, *Colloids Surf., A*, **354**, 291–297, 2010.
(16) M. Dirand, G. Martinoty and D. Langevin, Liquid Flow Through Aqueous Foams from Plateau Border Dominated Regime to Node Dominated Regime, *Phys. Rev. E.*, **60**, R6307, 1999.
(17) A. Saint-Jalmes, M. Peugeot, H. Ferraz and D. Langevin, Physical Chemistry in Foam Drainage and Coarsening, *Colloids Surf., A*, **263**, 219, 2005.
(18) A. Saint-Jalmes, Physical Chemistry in Foam Drainage and Coarsening, *Soft Matter*, **2**, 836–849. 2006.
(19) P. M. Kruglyakov, S. I. Karakashev, A. V. Nguyen and N. G. Vilkova, Foam Drainage, *Curr. Opin. Colloid Interface Sci.*, **13**,163–170, 2008.
(20) A. Schudko, *Colloid Chemistry*, Elsevier, Amsterdam, 1966.
(21) K. Khristov and D. Exerowa, Influence of the Foam Film Type on the Foam Drainage Process, *Colloids Surf., A*, **94**, 303–309, 1995.
(22) J. A. Kitchener in D. F. Danielli et al., Eds., In *Recent Progress in Surface Science*, Vol **1**, Academic Press, New York, 1964.
(23) A. Prins, Principles of Foam Stability. In *Advances in Food Emulsions and Foams*, Ed. E. Dickenson and G. Stainby, Elsevier Applied Science, London, 1988.
(24) R. Farajzadeh, R. Krastev and P. L. Z. Zitha, Foam Film Permeability; Theory and Experiment, *Adv. Colloid Interface Sci.*, **137**, 27–44, 2008; R. Farajzadeh, R. M. Muruganathan, W. R. Rossen and R. Krastev, Effect of Gas Type on Foam Film Foam Film Permeability; and Its Implications in Foam Flow in Porous Media, *Adv. Colloid Interface Sci.*, **168**, 71–78, 2011.
(25) A. J. De Vries, Foam Stability. Part 1. Structure and Stability of Foams, *Recueil*, **77**, 81, 81–91, 1958.
(26) A. Prins, Theory and practice of Formation and Stability in Food Emulsions and Foams, *Royal Society of Chemistry Publication*, Ed. E. Dickenson, London, 1987.
(27) D. Georgieva, A. Cagna and D. Langevin, Link between Surface Elasticity and Foam Stability, *Soft Matter*, **5**, 2063–2071, 2009.
(28) G. Andreatta, L.-T. Lee, F. K. Lee and J.-J. Benattar, Gas Permeability in Polymer and Surfactant Stabilized Bubble Films, *J. Phys. Chem. B.*, **110**, 19537–19542, 2006.
(29) A. G. Brown, W. C. Thuman and J. W. Mc Bain, Transfer of Air through Adsorbed Films as a Factor in Foam Stability, *J. Colloid Sci.*, **8**, 508–519, 1953.
(30) H. M. Princen and S. G. Mason, Shape of a Fluid Drop at a Fluid-Liquid Interface 1. Extension and Test of Two-Phase Theory, *J. Colloid Sci.*, **20**, 156–172, 1965.
(31) H. M. Princen, T. G. Overbeek and S. G. Mason, The Permeability of Soap Films to Gases II A Simple Mechanism of Monolayer Permeability, *J. Colloid Sci.*, **24**, 125–130, 1967.
(32) R. J. Archer and V. K. La Mer, The Rate of Evaporation of Water through a Fatty Acid Monolayer, *J. Phys. Chem.*, **59**, 200–208, 1955.
(33) P. P. N. Quoc, P. L. J. Zitha and P. K. Currie, Effect of Foam Film on Gas Diffusion, *J. Colloid Interface Sci.*, **248**, 467–476, 2002.

(34) R. Farajzadeh, R. Krastev and P. L. Z. Zitha, Gas Permeability of Foam Films Stabilized by an Alpha-Olefin Surfactant, *Langmuir*, **25** (5), 2883–2886, 2009.
(35) R. Krustev, D Platikanov and M. Nedyalkov, Permeability of Common Black Films to Gas Part 1, *Colloids Surf., A*, **79**, 129–136, 1993.
(36) M. Nedyalkov, R. Krustev, A. Stankova and D. Platikanov, Mechanism of Permeability of Gas through Newton Black Films at Different Temperatures, *Langmuir*, **8**, 3124–3144, 1992.
(37) R. Krustev, D. Platikanov and M. Nedyalkov, Permeability of Common Black Films to Gas Part 2, *Colloids Surf., A*, **123**–124, 383–390, 1997.
(38) R. M. Muruganathan, R. Krastev, H.-J. Muller and H. Mohwald, Foam Films Stabilized with Dodecyl Maltoside 2. Film Stability and Gas Permeability, *Langmuir*, **22**, 7981–7985, 2006.
(39) H. J. Muller, A Theory of Interactions by Changes of Interfacial Excess Quantities Mediated by Classical Long Range Forces. H. J. Muller, *Langmuir*, **14**, 6789–6792, 1998. R. Krustev and H.J. Muller Effect of Film Energy on gas Permeability on foam Films, Langmuir, 15(6), 2134–2141, 1999.
(40) Cited by R. Farajzadeh, R. Krastev, P. L. Z. Zitha, Foam Film Permeability: Theory and Experiment, *Adv. Colloid Interface Sci.*, **137**, 27–44, 2008.
(41) R. M. Muruganathan, H.-J. Muller, H. Mohwald and R. Krastev, Effect of Headgroup Size on Permeability of Neutron Black Films, *Langmuir*, **21**, 12222–12228, 2005.
(42) S. Hilgenfeldt, S. A. Koehler and H. A. Stone, Dynamics of Coarsening Foams-Accelerated and Self-Limiting Drainage, *Phys. Rev. Lett*., **86**, 4704, 2001; Focus: Foamy Flows, *Phys. Rev.*, **7**, 22, 2001.
(43) S. Saha, B. Bhaumik and A. Roy, Coupling between Drainage and Coarsening in Wet Foam, *Pramana, J. Physics*, **72** (6), 1037–1044, 2009.
(44) J. Boos, W. Drenckhan and C. Stubenrauch, On How Surfactant Depletion during Due Foam Generation Influences Foam Properties, *Langmuir*, **28**, 9303–9310, 2012.
(45) The Foam Scan Apparatus, IT Concept, Longessaigne, France, http://www.teclis-instruments.com/index.php/en/offer/products/foam-analyzer/foamscan, 2014.
(46) S. S. Dukhin, V. I. Kovalchuk, E. V. Arsenenko and R. Miller, Surfactant Accumulation within the Top Foam Layer Due to Rupture of External Foam Films, *Adv. Colloid Interface Sci.*, **137**, 45–56, 2008.
(47) D. Exowera and P.M. Kruglyakov, *Foam and Foam Films*, Elsevier Publications, 1997.
(48) T. Tamura, Y. Kaneko and M. Nikaido, Stability Factors of Foam Films in Contrast to Fluctuations Induced by Humidity Reduction, *J. Colloid Interface Sci.*, **190**, 61–70, 1997.
(49) X. Li, R. Shaw and P. Stevenson, Effect of Humidity on Dynamic Foam Stability, *Int. J. Miner. Process.*, **94**, 14–19, 2010.
(50) X. Li, S. I. Karakashev, G. M. Evans and P. Stevenson, Effect of Environmental Humidity on Static Foam Stability, *Langmuir*, **28**, 4060–4068, 2012.